

This manuscript is a **preprint** uploaded to EarthArXiv. This preprint version of the manuscript has not undergone peer-review. Subsequent versions may therefore have different content. The authors welcome comments and feedback via j.robertson@praxisuk.co.uk

1 **Distributed normal faulting in the tip zone of the South Alkyonides Fault System,**
2 **Gulf of Corinth, constrained using ³⁶Cl exposure dating of Late-Quaternary wave-cut**
3 **platforms.**

4
5 J. Robertson^{a*}, G.P. Roberts^a, F. Iezzi^a, M. Meschis^a, D. M. Gheorghiu^b, D. Sahy^c, C. Bristow^d, C.
6 Sgambato^e

7 ^aDepartment of Earth and Planetary Sciences, Birkbeck College, University of London, WC1E
8 7HX, UK.

9 ^bScottish Universities Environmental Research Centre, UK

10 ^cBritish Geological Survey, Keyworth, NG12 5GG, United Kingdom

11 ^dArcadis Consulting Ltd, London, UK

12 ^eInstitute for Risk and Disaster Reduction, University College London, London, UK

13
14 Corresponding author: Jenni Robertson (j.robertson@praxisuk.co.uk)

15
16 **Highlights**

- 17 • New age controls from Cape Heraion show wave-cut platforms are linked to 125 ka
18 • Distributed faulting has deformed wave-cut platforms since 125 ka
19 • High summed throw rates in the fault tip zone may be linked to fault interaction
20 • Deformation rates from tip zones are needed for fault based hazard assessment

21
22 **Abstract**

23

24 In order to investigate the geometry, rates and kinematics of active faulting in the region close
25 to the tip of a major crustal-scale normal fault in the Gulf of Corinth, Greece, we have mapped
26 faults and dated their offsets using a combination of $^{234}\text{U}/^{230}\text{Th}$ coral dates and *in situ* ^{36}Cl
27 cosmogenic exposure ages for sediments and wave-cut platforms deformed by the faults. Our
28 results show that deformation in the tip zone is distributed across as many as eight faults
29 arranged within ~700 m across strike, each of which deforms deposits and landforms
30 associated with the 125 ka marine terrace of Marine Isotope Stage 5e. Summed throw-rates
31 across strike achieve values as high as 0.3-1.6 mm/yr, values that are relatively high compared
32 to that at the centre of the crustal-scale fault (2-3 mm/yr from Holocene palaeoseismology
33 and 3-4 mm/yr from GPS geodesy). The relatively high deformation rate and distributed
34 deformation rate in the tip zone are discussed in terms of stress enhancement from rupture
35 of neighbouring crustal-scale faults and in terms of how this should be considered during
36 fault-based seismic hazard assessment.

37

38

39 1. Introduction

40 Understanding the deformation that occurs at the tips of normal faults is important
41 because (a) it contributes to knowledge on fault growth and linkage (e.g Cowie and Shipton,
42 1998; Peacock and Sanderson, 1991; McLeod et al., 2000; Peacock, 2002), (b) has the
43 potential to inform fault-based seismic hazard analysis about fault connectivity and maximum
44 rupture extent (Scholz and Gupta, 2000), and (c) influences our understanding of fluid
45 connectivity or otherwise of faulted hydrocarbon reservoirs (Yielding et al., 1996). One of the
46 key observations from studies on tip-zone deformation is that the shape of the displacement
47 gradients differs between isolated and interacting faults as a result of perturbation to the

48 surrounding stress field (Peacock and Sanderson, 1991; Willemse et al., 1996; Cartright and
49 Mansfield, 1998; Cowie and Shipton, 1998; Scholz and Lawler, 2004). In particular, steeper
50 displacement gradients occur close to fault tips where adjacent faults are in close proximity
51 (Gupta and Scholz, 2000). However, it is not known how these steep displacement gradients
52 develop through time, whether displacement is always localised on a single fault or spread
53 across several fault strands, and how tip deformation should be incorporated into studies of
54 seismic hazard. To answer these questions, this paper provides measurements of
55 deformation rates across all faults within a tip zone over timescales that allow one to
56 recognise how many individual faults are active simultaneously.

57 Our interest was raised for this topic because we note that at the tips of some crustal-
58 scale faults, distributed faulting dominates as networks of splay faults that form at acute
59 angles to the main fault (McGrath and Davison, 1995; Perrin et al., 2016) (Figure 1). It is
60 unclear whether these fault patterns and the resultant deformation can be more complex
61 where the tips of two crustal-scale faults overlap along strike and interaction occurs between
62 neighbouring faults (Gupta and Scholz, 2000). Moreover, although typically fault
63 displacement decreases to minimal values toward the tip (Cowie and Roberts, 2001), a shared
64 tip zone can host high displacement gradients relative to the main fault (Peacock and
65 Sanderson, 1991; 1994; Schlische et al., 1996) and it is unclear if this is accommodated by
66 deformation spread across multiple faults or localised on a single fault.

67 A detailed analysis of the deformation within a fault tip zone has the capacity to
68 contribute to fault-based seismic hazard assessment (e.g. Pace et al., 2016). If tip zones
69 contain relatively-high displacements, distributed across multiple faults, or localised on a
70 single fault, this may influence whether ruptures can cross the tip zone onto other
71 neighbouring faults (e.g. Field et al. 2014), influencing estimates of maximum earthquake

72 magnitude (Wells and Coppersmith, 1994). However, the lack of measured displacement data
73 within tip zones means that historic fault-based seismic hazard approaches typically rely on
74 throw/slip rate data from outside the tip zone and the assumption that displacement
75 gradients decrease toward the tips according to pre-ordained fault shapes (Faure Walker et
76 al., 2018). The above assumptions produce significant uncertainty in PSHA (Pace et al., 2016),
77 and have been shown to result in large differences between calculations of recurrence
78 intervals and ground-shaking exceedance probabilities for different fault geometries (Faure
79 Walker et al., 2018). Constraining the rates of deformation at multiple locations along a fault,
80 including within the tip-zone, is therefore a vital component of reducing the uncertainty in
81 PSHA. Furthermore, this may be particularly important if this analysis is carried out in an area
82 where overlapping tip zones occur; higher displacement gradients, and consequently
83 slip/throw rates, may mean that cumulative slip rates may be relatively high, even when
84 compared to 'on fault' values.

85 One of the main challenges to gaining insights of how tip-zone deformation
86 accumulates through time, over timescales relevant to earthquake rupture, is to derive
87 knowledge of the timescales over which faulting occurs. Existing approaches use
88 measurements of vertical displacement, coupled with the ages of offset strata/landforms (e.g.
89 Sieh et al. 1989; Armijo et al. 1991; Roberts and Michetti, 2004; Galli et al., 2008; Schlagenhauf
90 et al., 2010, Mozafari et al. 2019; Robertson et al., 2019). In tip zones where distributed
91 faulting dominates and slip-rate along individual faults may be (a) relatively low, and (b)
92 difficult to detect, it may be advantageous to concentrate on techniques that average the slip
93 over relatively long time periods. Investigations using deformed Quaternary marine terraces
94 and their associated wave-cut platforms (e.g. Armijo et al., 1996; Roberts et al., 2009, Roberts
95 et al., 2013; Binnie et al., 2016; Jara-Munoz et al., 2017; Meschis et al., 2018; Robertson et al.,

96 2019) allow deformation rates to be measured over 10^{4-5} years, and therefore displacement
97 associated with the very low slip rates of individual tip-zone faults can be resolved.

98 The western tip area of the north dipping South Alkyonides Fault System (SAFS)
99 (Morewood and Roberts, 1997), located on the Perachora Peninsula (eastern Gulf of Corinth,
100 Greece) provides an opportunity to study the throw rate, 'off-fault' deformation and possible
101 interaction with neighbouring faults. A set of distributed faults at Cape Heraion, in the far
102 west of the Perachora Peninsula, represents the western tip zone of the SAFS (Morewood and
103 Roberts, 1997) (Figure 2). While this area has been studied before (Morewood and Roberts,
104 1997), this study lacked the detailed mapping of displacement gradients along individual
105 faults, and the age constraints needed to be able to fully examine the rates and spatial
106 variation of deformation. Morewood and Roberts (1997) identified faulted offsets of what
107 they claim is a single marine terrace. Others have made an alternative interpretation where
108 marine terraces at different elevations are not faulted, but rather date from different sea-
109 level highstands (Leeder et al., 2003; Leeder et al., 2005). This disagreement could not be
110 resolved, because although some age constraints were available from $^{234}\text{U}/^{230}\text{Th}$ dating of
111 corals (Vita-Finzi et al., 1993, Leeder et al., 2003; Leeder et al., 2005; Roberts et al., 2009;
112 Houghton, 2010), ages were not available for marine terrace deposits at different elevations.

113 Our breakthrough reported herein, is that our detailed mapping revealed that the
114 coral-bearing strata can be mapped along strike into wave-cut platforms, and wave-cut
115 platforms can be dated using in situ ^{36}Cl cosmogenic exposure studies (Robertson et al. 2019).
116 Here we test the hypothesis of Morewood and Roberts (1997) of a single, faulted
117 palaeoshoreline by (i) constraining the ages of marine terrace deposits and landforms at
118 different elevations, (ii) calculating individual and cumulative fault throw values and, (iii)
119 exploring how these vary spatially within the tip zone and how they compare to other normal

120 fault tip zones. The results of these analyses are combined with those from Coulomb stress
121 change modelling to explore the interaction of the tip of the SAFS with neighbouring faults.
122 These findings are then discussed in the context of fault-based probabilistic seismic hazard
123 assessment.

124

125 **2. Background**

126

127 *2.1 Tectonic setting*

128 The Perachora Peninsula is located within the eastern Gulf of Corinth (Figure 2), one
129 of the world's fastest extending rift systems, with extension rates between <5 mm/yr and 10-
130 15 mm/yr (Davies et al., 1997; Clarke et al., 1998; Briole et al., 2000). The presence of a
131 complex basin structure (e.g. Moretti et al., 2003; Sachpazi et al., 2003; McNeill et al., 2005;
132 Sakellariou et al., 2007; Bell et al., 2009; Nixon et al., 2016; Gawthorpe et al., 2018) is a
133 consequence of extension accommodated along sets of north and south dipping faults. From
134 the Late Quaternary to the present day north-dipping faults located along the rift system that
135 borders the south of the gulf are predominately responsible for extension with other faults
136 less active or ceasing activity (Sakellariou et al., 2007; Bell et al., 2009; Roberts et al., 2009;
137 Nixon et al., 2016; Fernandez-Blanco et al., 2019). The north-dipping faults have been shown
138 to have started to dominate the deformation between 340-175 ka (Roberts et al., 2009; Nixon
139 et al., 2016).

140 The Perachora Peninsula is located between the Alkyonides Gulf to the north and the
141 Lechaion Gulf to the south (Figure 2a). This area is dominated by two crustal-scale, north-
142 dipping, active fault systems, the East Xylocastro Fault System (EXFS) (so named in this study)
143 and the South Alkyonides Fault System (SAFS) (Figure 2a). The EAFS is formed by the East

144 Xylocastro, North Kiato and Perachora faults, located offshore and arranged en-echelon. The
145 linkage of these three faults is unclear (Bell et al., 2009) with some authors suggesting fault
146 connections at depth (Armijo et al., 2006; Nixon et al., 2016) and others suggesting that they
147 are isolated faults (Stefatos et al., 2002; Moretti et al., 2003; Sakellariou et al., 2007). The
148 presence of a set of coherent terraces in the footwall of the East Xylocastro, North Kiato and
149 Perachora faults (Armijo et al., 2006) combined with the formation of a single depocentre
150 bounding the north-dipping faults on the south side of the gulf (Nixon et al., 2016) has been
151 cited as evidence to support a through-going fault that is connected at depth.

152 The predominantly onshore, ~40 km long SAFS is comprised of the Pisia, Skinios, East
153 Alkyonides and Psatha faults (Figure 2, Roberts, 1996a; Morewood and Roberts, 1997; 1999;
154 2001; 2002; Leeder et al., 2005; Roberts et al., 2009). Analysis of the fault system shows that
155 slip vectors converge toward its centre (Roberts, 1996a; Roberts, 1996b) where a maximum
156 cumulative throw of 2500 m is recorded (Morewood and Roberts, 2002), which decreases
157 toward both tips (Roberts, 1996a; Morewood and Roberts, 1999; Roberts et al., 2009). In the
158 western section of the SAFS, decreasing offset is reflected in deformed Late Quaternary
159 palaeoshorelines and Holocene notches in the footwall (Cooper et al., 2007; Roberts et al.,
160 2009), where uplift rates decrease from 0.52 mm/yr to 0.25 mm/yr from east to west in the
161 most western 5 km of the fault. Roberts et al. (2009) identified that the SAFS experienced an
162 increase in slip rate since ~175 ka by a factor of ~3, suggested to be linked to the cessation of
163 faulting on neighbouring across-strike faults.

164 Evidence from recent earthquakes combined with Holocene throw and slip rate data
165 provide insight into the activity of faults within the SAFS over decadal to 10^3 year timescales.
166 Specifically, analysis of post-LGM slip on the Pisia fault revealed maximum slip rates of 2.3
167 mm/yr during the Holocene (Mechernich et al., 2018). Palaeoseismic trenching along the

168 Skinos fault yielded throw rates of 1.2-2.5 mm/yr over ~1500 years (Collier et al., 1998). Two
169 >Ms 6 earthquakes on the 24th and 25th February 1981 are reported to have partially ruptured
170 faults within the SAFS (Jackson et al., 1982; Roberts, 1996a; Collier et al., 1998). Ruptures in
171 bedrock and alluvium that extend for 15-20 km (Jackson et al., 1982; Bornovas et al., 1984;
172 Roberts, 1996a) were observed following the February 1981 earthquakes, with maximum
173 coseismic throw values of 150 cm and 100 cm identified on the Pisia and Skinos faults
174 respectively (Jackson et al., 1982).

175 The February 1981 earthquake ruptures were mapped to a throw minima along the
176 south of Lake Vouliagmeni (Figure 2c) (Bornovas, 1984; Roberts, 1996a; Morewood and
177 Roberts, 1999) where the “throw and geomorphic expression across [the SAFS] tend to zero”
178 (Morewood and Roberts, 1999) and were used to conclude that the SAFS does not extend
179 beyond the western end of the lake. Consequently, this location was identified as the western
180 fault tip of the SAFS (Morewood and Roberts, 1999, Figure 4a) (‘A’ on Figure 2c). The area to
181 the west of this location, Cape Heraion, is deformed by numerous normal faults, providing an
182 excellent opportunity to explore deformation close to the tip of a normal fault.

183

184 *2.2 Cape Heraion, Perachora Peninsula*

185 The extreme west of the Perachora Peninsula, Cape Heraion, is located beyond the
186 western tip of the SAFS (as defined by Morewood and Roberts, 1999, Figure 2c). It is bounded
187 to the north by the Perachora fault segment, the most eastern fault within the EXFS, and to
188 the south by the south dipping, active Heraion fault (Taylor et al., 2011; Charalampakis et al.,
189 2014; Nixon et al., 2016) (Figure 2a). The geology of Cape Heraion is comprised of a succession
190 of deposits from the Mesozoic to the Late Quaternary with more recent Late Quaternary-

191 Holocene geomorphic features imprinted such as wave-cut platforms and Holocene sea-level
192 notches.

193 The stratigraphic succession of the Cape comprises Mesozoic basement limestones
194 unconformably overlain by Plio-Pleistocene marls and sandstones that are, in turn, overlain
195 by algal mound bioherms (also known as cyanobacterial mounds) above which a bioclastic
196 shallow-marine coral-bearing sediment occurs (Bornovas, 1984; see Portman et al., 2005 for
197 descriptions of each lithology). The bioherms are dominated by freshwater branched
198 cyanobacterium *Rivularia haematites*, suggested to have formed when the Gulf of Corinth
199 was a lake (Kershaw and Guo, 2001, 2003, 2006). Domal-topped bioherms in the hangingwall
200 and flat-topped bioherms in the footwall suggest they grew up to water level during faulting
201 with restricted vertical growth in the footwall (Kewshaw and Guo, 2006). Subsequent relative
202 sea-level rise resulted in the presence of a marine bioclastic layer above the bioherms
203 (Portman et al., 2005; Roberts et al., 2009) and caves containing marine biota within the
204 bioherms (Kershaw and Guo, 2006). Taken together, the above evidence is suggestive that
205 faults were active during initial freshwater conditions, that were subsequently changed to
206 marine by a relative sea-level rise. However, these lines of evidence are debated by other
207 authors (Leeder et al., 2005; Portman et al., 2005; Andrews et al., 2007), who favour that the
208 bioherms grew in a marine environment.

209 The observed geomorphology on Cape Heraion resembles that of a 'stepped' profile
210 with horizontal surfaces (terraces) separated by steep slopes. The sub-horizontal surfaces are
211 interpreted as marine terraces because they are associated with coralliferous sediments,
212 marine shoreface deposits with Quaternary marine fossils, and wave-cut platforms that are
213 commonly bored by marine lithophagid borings (Morewood and Roberts, 1997, 1999; Leeder
214 et al., 2003; Leeder et al., 2005; Roberts et al., 2009). Quaternary marine terraces typically

215 form during glacio-eustatic sea-level highstands that occur as a response to glacial melting
216 during interglacial periods. At the up-dip terminations of the marine terraces, it is common to
217 find wave-cut notches and platforms that host features such as lithophagid borings and inter-
218 tidal millholes, indicative of formation at palaeoshorelines (Westaway 1993; Griggs et al.,
219 1994; Miller and Mason, 1994; Roberts et al., 2009; Robertson et al., 2019).

220 Although the marine terraces and intertidal palaeoshoreline indicators are widely
221 accepted, the explanation for the steep slopes separating marine terraces is debated on Cape
222 Heraion. The slopes are interpreted in two ways by different authors: (1) as palaeo- sea-cliffs,
223 cut by wave-action by three successive Quaternary glacioeustatic sea-level highstands
224 (Leeder et al., 2003; Leeder et al., 2005) (Figure 3a); (2) the locations of faults offsetting a
225 single terrace surface, where the up-dip termination of a terrace surface at a slope is the
226 hangingwall cut-off of the marine terrace along the fault (Figure 3b; Morewood and Roberts,
227 1997). In this latter interpretation, the age of the marine terrace is suggested to be ~125 ka,
228 associated with MIS 5e (Morewood and Roberts, 1997; Roberts et al., 2009) (Figure 3b), with
229 the presence of complex faulting representing a Segment Boundary Zone between the EXFS
230 and SAFS. Both of these explanations rely on age constraints that link a wave-cut platform at
231 ~29 m to MIS 5e (125 ka highstand) dated using U-series coral ages (Vita-Finzi et al., 1993,
232 Leeder et al., 2003; Leeder et al., 2005; Houghton, 2010) (Locality F, Figure 4a), but no age
233 constraints have been available for higher elevation examples, and this is needed to
234 differentiate between the competing hypotheses.

235 We undertook detailed mapping and dating in an attempt to resolve the debate of
236 successive palaeoshorelines versus faults. In particular, we tried to identify whether the
237 slopes between terrace locations were continuous along strike, consistent with the
238 suggestion that they represent a succession of palaeoshorelines, or whether the offset of the

239 slopes varied along strike and displayed tip zones and relay ramps, suggestive of faulting.
240 Later we present the results of field mapping and dating that supports the hypothesis of
241 Morewood and Roberts (1997) that the observed variation in terrace elevation is as a result
242 of faulting.

243 The significance of Holocene wave-cut notches cut into the cliffs along the most
244 western point of Cape Heraion has also been the subject of debate (Pirazzoli et al., 1994;
245 Stiros, 1995; Stiros and Pirazzoli, 1998; Kershaw and Guo, 2001; Cooper et al., 2007; Boulton
246 and Stewart, 2015; Schneiderwind et al.,2017a; Schneiderwind et al.,2017b). It is clear that
247 these notches form as a result of the chemical, biological and physical wave action eroding
248 the cliffs in the intertidal zone along palaeoshorelines (Pirazzoli, 1986). The ages of four
249 notches observed on Cape Heraion were dated to between 190-440 A.D. and 4440-4320 A.D.
250 and used to infer coseismic footwall uplift increments of 0.8 m from earthquakes with
251 recurrence intervals of ~1600 years (Pirazzoli et al., 1994). However, 0.8m has been suggested
252 to be a relatively high value for coseismic footwall uplift (Cooper et al., 2007; Boulton and
253 Stewart, 2015; Schneiderwind et al.,2017b; Meschis et al., 2019). Whatever their mode of
254 formation, we show below that the notches are deformed by active faulting and use this as
255 part of our explanation of the geological history of Cape Heraion.

256

257 *2.3 Using marine terraces and wave-cut platforms to obtain age constraints*

258 Exploring the deformation of marine terraces and wave-cut platforms relies on
259 obtaining age controls for terraces, accurate geomorphic mapping of terrace features and
260 knowledge of the timing and relative elevations of sea-level highstands (Robertson et al.,
261 2019). Existing coral ages on Cape Heraion at localities C and F (Figure 4a) dated using
262 $^{234}\text{U}/^{230}\text{Th}$ dating reveal ages that agree to coral growth during MIS 5e from a platform at 7 m

263 (Roberts et al., 2009) and a platform at 29 m (Collier et al., 1992; Vita-Finzi et al., 1993; Leeder
264 et al., 2003; Leeder et al., 2005; Dia et al., 2007; Houghton, 2010). To augment these ages,
265 this study provides new coral ages, and *in situ* ^{36}Cl cosmogenic exposure ages for wave-cut
266 platforms, inspired by the work of Stone et al. (1996), that can be mapped along strike onto
267 coral-bearing marine terrace sediments. The ^{36}Cl cosmogenic exposure ages will be cross
268 checked against new and existing coral ages.

269 Integral to studies of Quaternary marine terraces and palaeoshorelines is knowledge
270 of sea-level elevation changes linked to sea-level highstands, and the time when sea-level
271 reached its maximum elevation (e.g. Waelbroeck et al., 2002; Lambeck et al., 2002; Siddall et
272 al., 2003; Grant et al., 2014; Spratt and Lisiecki, 2016). On Cape Heraion existing coral ages
273 constrain two wave-cut platforms to MIS 5e (125 ka sea-level highstand) (Localities C and F,
274 Figure 4a). The timing of MIS 5e occurred between 138-116 ka (Muhs and Szabo, 1994; Stirling
275 et al., 1998; Hearty et al., 2007; O’Leary et al., 2013; Dutton et al., 2015), with the majority
276 (80%) of sea-level rise suggested to have occurred prior to 135 ka (Muhs and Szabo, 1994;
277 Gallup et al., 2002). Understanding the elevations and timings of past sea levels is beneficial
278 because it provides an additional check against the ages obtained from ^{36}Cl exposure dating,
279 which should fall within known highstand time periods.

280

281 3. Methods

282

283 3.1 Field mapping

284 Detailed field mapping and sampling for $^{234}\text{U}/^{230}\text{Th}$ and *in-situ* ^{36}Cl exposure dating
285 was carried out during field campaigns throughout 2015 and 2017. For the field mapping we
286 concentrated on key criteria that would differentiate between the palaeo-sea-cliff versus fault

287 interpretations for the steep slopes between terrace locations. In particular, if the steep
288 slopes are palaeo- sea-cliffs they ought to be continuous along strike (Figure 3b). In contrast,
289 if the steep slopes are fault scarps, they may display relay-zone geometries where it would be
290 possible to walk continuously on a single surface, along strike, around fault tips, up relay
291 ramps onto the higher parts of the same terrace surface (Figure 3b).

292 In order to constrain the geometries and continuity of the marine terraces (Figure 3),
293 58 spot-height elevations were measured throughout the field area using a handheld
294 barometric altimeter (3 m vertical error) that was regularly calibrated at sea level. These
295 measurements were supplemented by 40 additional elevation values obtained from a 5 m
296 digital elevation model (DEM) (4 m vertical error). The combination of spot heights, outer
297 edges and fault trace maps has allowed us to identify displacement gradients, fault tips to
298 individual faults and relay zones separating individual faults. Rupture traces from recent
299 (possibly 1981) faulting were mapped using a barometric altimeter and measured with rulers
300 to identify the vertical offsets (throw) observed in colluvium and on bedrock fault scarps and
301 the horizontal extension observed from piercing points. This was carried out as per the
302 approach outlined in lezzi et al. (2018).

303

304 3.2 $^{234}\text{U}/^{230}\text{Th}$ sampling approach and preparation

305 We focussed our attention on a 0.5-1 m thick coral-bearing, bioclastic layer overlying
306 the bioherms. The bioclastic deposits are comprised of coarse sand and contain corallites of
307 *Cladocora caespitosa*. Whole corallite samples were removed and prepared as per the
308 approach outlined in Roberts et al. (2009). Each corallite sample was split and the septa
309 removed and discarded as septa have been shown to experience greater post-depositional
310 alteration (Roberts et al., 2009; Houghton, 2010). Individual samples were then fragmented

311 and analysed under a binocular microscope for signs of alteration that appear as patches of
312 brown colouration and small crystal growths. The corallites were physically cleaned using a
313 scalpel to remove areas of alteration and any sediment and then placed in 10% hydrochloric
314 acid for 2-3 seconds after which they were immediately rinsed in ultrapure water. This process
315 was repeated until all signs of alteration were removed. Following this process fragments
316 from each corallite were analysed for $^{234}\text{U}/^{230}\text{Th}$ as per the method detailed in Crémière et al.
317 (2016).

318

319 *3.3 ^{36}Cl sampling approach and preparation*

320 For ^{36}Cl dating we focussed our attention on wave-cut platforms that could be mapped
321 along and across strike into the coral-bearing, bioclastic layer, suggesting they would be close
322 in age. Obtaining the absolute ages of wave-cut platforms using cosmogenic ^{36}Cl exposure
323 dating relies on (i) sampling from a surface comprised of a calcium-rich lithology that has (ii)
324 experienced minimal erosion since exposure. This is because the primary production pathway
325 of cosmogenic ^{36}Cl occurs when ^{40}Ca undergoes spallation following the collision of high-
326 energy neutrons at the earth's surface (Dunai, 2010). The spallation reaction is mostly limited
327 to the upper 2 m of rock below exposed surfaces, decreasing exponentially with depth
328 (Licciardi et al., 2008), so high levels of erosion would remove the highest concentrations
329 producing misleadingly-young ages. Other pathways of ^{36}Cl production that must be
330 considered are from low-energy neutrons (Schimmelpfennig et al., 2009) and negative
331 muons, which are the dominant production mechanism for ^{36}Cl at greater depths (Dunai,
332 2010). We use the approach outlined in Robertson et al. (2019) to identify surfaces that have
333 experienced minimal erosion based on the presence of preserved lithophagid borings and
334 millholes. The depth of lithophagid borings upon formation is between 3-9 cm (Peharda et al.,

335 2015) while millholes, that is, erosional hollows formed by pebble agitation in the intertidal
336 zone, are usually a few centimeters to a few decimetres deep. Therefore, the preservation of
337 these features allows us to be confident that we can constrain erosion to less than a few
338 millimetres or centimetres. The low rates of erosion mean that the ^{36}Cl concentration depth
339 profile, determined by the ^{36}Cl production rate depth variation from spallation, will be intact
340 and amenable to age derivation using modelling.

341 We sampled from wave-cut platforms comprised of differing lithologies at a range of
342 elevations: 62 m, 60 m, 46 m, 42 m and 29 m, including one location where there is existing
343 age control from $^{234}\text{U}/^{230}\text{Th}$ coral ages (Locality F, Figure 4a) from sediments formed quasi-
344 contemporaneously with the wave-cut platform (Vita-Finzi et al., 1993; Leeder et al., 2003;
345 Leeder et al., 2005; Houghton, 2010). All samples were removed using a mallet and chisel.
346 Shielding values were noted every 30° of azimuth (as per the method in Dunai, 2010), and
347 used in the age exposure calculations to account for the shielding of cosmogenic rays on the
348 sample site by the surrounding topography (Dunai, 2010). Following removal, samples were
349 analysed in thin section to determine their lithology, washed in distilled water in an ultrasonic
350 bath, then crushed and prepared for ^{36}Cl exposure dating using Accelerator Mass
351 Spectrometry (AMS) as per the method outlined by Schimmelpfennig et al. (2009). The data
352 obtained from AMS was input into CRONUScalc (Marrero et al., 2016), an online calculator
353 that uses measured inputs from data such as ^{36}Cl concentration, elemental composition,
354 elevation, shielding, water content and appropriate uncertainties to calculate the age of the
355 samples with uncertainty values attached.

356

357 4. Results

358

359 This section explores the results of our detailed geological mapping of Cape Heraion
360 and the absolute ages obtained from our ^{36}Cl cosmogenic exposure dating and $^{234}\text{U}/^{230}\text{Th}$
361 dating. Alongside existing published ages, these new absolute ages are used to constrain the
362 ages of surfaces at different elevations on Cape Heraion in order to show that faulting is
363 responsible for offsetting a marine terrace linked to the 125 ka highstand within MIS 5e. The
364 results of the dating are used to drive throw rate analyses in order to calculate cumulative
365 throw within the tip zone since 125 ka.

366

367 *4.1 Field mapping*

368 Detailed field mapping reveals complicated, but linked spatial relationships between
369 lithologies, the stratigraphy and geomorphic features on Cape Heraion (Figures 4, 5, Appendix
370 1, which contains a description of the stratigraphy). Wave-cut platform features have been
371 cut into the stratigraphy (Figure 4a) and are widespread throughout the cape at elevations
372 from 6 m to 99 m (Figures 4, 5 and 6). These horizontal to sub-horizontal surfaces exhibit
373 millholes and lithophagid borings, which are particularly well preserved on the platforms
374 composed of bioclastic packstone (Figures 4a, 6e). Associated with the wave-cut platforms,
375 several localities display coastal notches where the wave-cut platforms impinge on steep
376 outcrops. The notches are marked with lithophagid borings, for example close to location B
377 at ~41 m, with another notch observed at ~92 m (Locality J, Figure 4a).

378 Our mapping suggests that the lithologic, the stratigraphic and geomorphic features
379 can be interpreted as due to the effect of wave-erosion, at the time of wave-cut platform
380 formation, impinging on palaeo- Cape Heraion, characterised at that time by Quaternary
381 sediments onlapping onto an upstanding inlier of Mesozoic limestone (Figure 5b). The lateral
382 stratigraphic variations were denuded by the wave erosion so that the wave cut-platform

383 formed on different stratigraphic units across the mapped area. The stratigraphy, and the
384 wave-cut platform, have been subsequently offset by faulting that, therefore, post-dates the
385 wave-cut platform, the Cladocora-bearing bioclastic sands and the Rivularia-bioherms (Figure
386 7).

387 To gain further insights into the faulting, we have studied the steep slopes that occur
388 along the faults, and in particular the breaks of slope (Figure 4a, c). The map pattern produced
389 by the breaks of slopes reveals patterns that resemble displacement variations along the
390 faults, with slip maximum close to the centres of the map traces, and the positions of relay-
391 ramps at fault tips (Figure 4c). Hence, we interpret these breaks of slope to represent
392 hangingwall and footwall cut offs. Cross-sections across the faults are shown in Figure 8. To
393 cross-check the interpretation of fault segmentation in Figure 4c, we used the elevation data
394 shown in Figure 4b to measure the vertical offsets across the faults, checking that relay-ramps
395 and fault tips identified on Figure 4c are marked by decreased vertical offsets (Figure 9). This
396 cross-check confirms that locations where the hangingwall and footwall cut-offs converge in
397 map view (e.g. the relay-ramps and faults tips in Figure 9b have low or zero vertical offsets,
398 consistent with our fault segmentation model).

399 As a final check on the geometries of the faults we have compared their displacement
400 (d) to length (L) ratios to those in a global database (Schlische et al. 1996), because $d = \gamma L$,
401 where $\gamma = 0.01-0.1$ with a preferred value of 0.03. We have analysed faults where we have
402 identified both fault tips, and faults where we consider that the centre of the fault has been
403 mapped, assuming that the displacement profiles will be symmetrical. We find values of
404 γ between 0.01-0.1 (Table 1), suggesting that the vertical extents of the steep slopes
405 separating terrace locations are consistent with the interpretation that they are fault scarps.
406 The exception is fault 4, which has a d/L ratio that is comparatively higher (0.27), possibly as

407 a result of being linked at depth with faults 1 and 10 (see the individual fault throw profiles in
408 Figure 9a for faults 1, 4 and 10). Consequently, the combined d/L ratio of these three faults is
409 not representative because the fault continues offshore to the west (Figure 4a, b).

410 We describe the details of the faulting below. With the exception of three faults that
411 strike approximately N-S not considered in this study, all of the faults strike parallel-sub
412 parallel to the average 260° of the SAFS between 230° and 300° (Figures 2, 4). The faults in
413 the north of the cape are all north dipping and exhibit short fault lengths (100-400 m) and
414 offsets of 2-20 m. South of Fault 11 the presence of a north dipping fault is inferred owing to
415 the 20 m offset of bioherms observed along the scarp of fault 11 (Figure 4a, b). Faults along
416 the south of the cape are longer, and extend outside of the mapping area to the east and
417 offshore to the west (faults 1, 17 and 18) (Figures 4a-c, 7a-c). Along the south of the cape,
418 there are four south-dipping faults (1, 4, 10 and 18) (Figures 4b, 7a-c, e, f). The scarp of fault
419 18 is not accessible and the offset of this fault is a minimum value as its hangingwall is
420 offshore, however, this fault has been mapped by Morewood and Roberts (1999) farther to
421 the east for ~ 2 km. South dipping faults 1, 4 and 10 appear to be en echelon to one another
422 and exhibit limestone fault scarps that decrease in offset from west to east.

423 Strike and dip values, and, where visible, fault striations were measured along the
424 limestone fault scarps of Faults 1, 2, 10 and 17 (Figure 4d). The fault dip for these faults range
425 between $43-66^\circ$. In places faults display evidence of activity in a marine setting, faults 1 and
426 4 display post-slip marine cementation of submarine scree coating the faults (Scott, 1995).
427 Along north dipping faults 2 and 11, offset algal bioherms have horizontal lines of abundant
428 lithophagid borings at 34 m and 41 m respectively, again suggesting slip post-dates wave-cut
429 platform formation.

430 In summary, our geomorphological observations and elevation measurements
431 suggest that a pattern of distributed faulting is visible on Cape Heraion. In the context of the
432 north-dipping SAFS and its approximate E-W strike, the faulting on Cape Heraion displays a
433 set of synthetic and antithetic faults that display a 70° variation in strike. While north-dipping
434 faults are more numerous, they appear to have smaller lengths and offsets compared to the
435 four south dipping faults.

436

437 4.2 $^{234}\text{U}/^{230}\text{Th}$ coral dating

438 The *Cladocora caespitosa* corallites sampled from Cape Heraion (S6U/Th, S7U/Th)
439 (Figure 4) were removed from within a death assemblage on the 44 m wave-cut platform
440 predominantly composed of friable sediments (Figures 6b, 7a). Results of $^{234}\text{U}/^{230}\text{Th}$ dating on
441 S6U/Th and S7U/Th reveal growth ages of 137 ka and 136 ka respectively (Figure 8a, Table 2).
442 The age presented for S6U/Th is comprised of the average of three analyses from the same
443 corallite, a fourth age was also obtained from this corallite, but we have excluded it as the
444 age of 173.7 ky suggests that it is an outlier (Table 2). The average age of sample S7U/Th is
445 obtained from six analyses from the same corallite (Table 2). The $^{234}\text{U}/^{230}\text{Th}$ coral ages support
446 growth during MIS 5e and are similar to existing coral growth ages from Cape Heraion (Figure
447 8a; Vita-Finzi et al., 1993; Leeder et al., 2005; Roberts et al., 2009; Houghton, 2010). Note that
448 all samples have relatively high values of $\delta^{234}\text{U}$ of 191-214 (a common way to represent the
449 initial activity ratios of $^{234}\text{U}/^{238}\text{U}$) compared to modern seawater in the Gulf of Corinth (value
450 of 151; Roberts et al., 2009). It is expected that the samples should have $\delta^{234}\text{U}$ values similar
451 to modern sea-water. However, previous studies of coral ages in the Gulf of Corinth, which
452 successfully produced ages of independently-known glacio-eustatic sea-level highstands,
453 have tended to show elevated values (e.g. Collier et al., 1992; Vita-Finzi et al., 1993; McNeill

454 and Collier, 1994; Dia et al., 1997; Leeder et al., 2005; Roberts et al., 2009; Houghton, 2010;
455 Turner et al., 2010), probably due to the fact that it is a restricted basin with freshwater input.
456 The analyses herein also suggest an age similar to a well-known glacio-eustatic sea-level
457 highstand at ~125 ka. Thus, like previous studies, we use the implied age in our later analysis,
458 despite the relatively high initial activity ratio for our samples.

459

460 4.3 ³⁶Cl exposure dating of wave-cut platforms

461 Cosmogenic ³⁶Cl exposure dating is used to indicate the time period that sampled
462 surfaces have been subaerially exposed and thus accumulating significantly higher values of
463 ³⁶Cl compared to pre-exposure. Five samples were removed from limestone, bioclastic
464 packstone and algal bioherm wave-cut platforms at different elevations on Cape Heraion
465 (Figures 4a, 6). Our field observations are used to inform the erosion rate used as an input
466 parameter into CRONUScalc, which is used to calculate the exposure age of the samples. The
467 preservation of lithophagid borings and millholes on bioclastic packstone and limestone
468 surfaces (Figure 6) indicate total erosion values of much less than 0.2-0.3 m, whilst samples
469 from the tops of bioherms are expected to have experienced total erosional values similar
470 with the removed depth of bioclastic packstone eroded from the surface of ~0.6 m. These
471 limestone/packstone and bioherm values equate to erosion rates of 0.1 and ~6.0 mm/ky
472 respectively. The 0.1 mm/yr value is the same as that used on limestone wave-cut platforms
473 dated using ³⁶Cl exposure dating in south Crete (Robertson et al., 2019).

474 Assuming the erosion rates stated above are correct, the ³⁶Cl exposure ages of five
475 samples (Figure 8a, Table 3) are: S1 (limestone, sampled at 60 m) 122 ± 29 ka; S2 (bioherm,
476 sampled at 62m) 108 ± 36 ka; S3 (bioclastic packstone, sampled at 42 m) 109 ± 24 ka; S4
477 (bioherm, sampled at 46 m) 120 ± 40 ka; S5 (bioherm, sampled at 29 m) 112 ± 35 ka. These

478 results agree with the new and existing U-series ages presented above, suggesting late
479 Quaternary ages close to the age of the 125 ka highstand. The error bars on the ages appear
480 relatively-large, but are comprised of internal (analytical) and external (total) uncertainties
481 that are associated with measured input parameters into CRONUScalc (e.g. H₂O content,
482 elevation, shielding, erosion rates and the production rate; Marrero et al., 2016). Where
483 samples are removed from the same geographical location using the same method, the error
484 values of the input parameters used to calculate the external uncertainty will be very similar
485 (i.e shielding) or even the same (i.e production rate, elevation values). Consequently, Marrero
486 et al. (2016) suggests that the external uncertainty value linked to the exposure age may be
487 overestimated when comparing results from the same geographical area, sampled using the
488 same method (see Dunai, 2010). This possible overestimate or uncertainties should be borne
489 in mind when considering the relatively-large error bars associated with the exposure ages,
490 but we have chosen to report the full range of possible uncertainty herein.

491 We suggest that all our exposure ages for the wave-cut platform are associated with
492 MIS 5e, and we discuss this below. Our exposure age results link S1 and S4 and their
493 associated wave-cut platforms to MIS 5e, but the wave-cut platforms that S2, S3 and S5 were
494 removed from, might, at first sight, be linked to either MIS 5c (100 ka highstand) or MIS 5e
495 (125 ka highstand) (Figure 8a). However, using the exposure ages obtained from S1 (60 m)
496 and S4 (46 m), new ²³⁴U/²³⁰Th ages from S6 and S7 (44 m) and existing U-series dating of corals
497 on platforms at 7 m (Roberts et al., 2009) and 29 m (Vita-Finzi et al., 1993; Leeder et al., 2003;
498 Leeder et al., 2005; Houghton, 2010) alongside sea-level curve data we suggest that it is more
499 likely that S2 (62 m), S3 (42 m) and S5 (29 m) are associated with MIS 5e (Figure 8c). Our
500 reasoning is that it is difficult to reconcile that platforms at 60 m, 46 m, 44 m, 29 m and 7 m
501 were formed by the MIS 5e 125 ka highstand, yet platforms at similar elevations (62 m, 46 m

502 and 29 m) were formed by the MIS 5c 100 ka highstand. This is especially unlikely, given that
503 the maximum sea level during the 100 ka highstand in MIS 5c was -25 m relative to today, and
504 this is 30 m lower than the 5 m relative sea level during the 125 ka highstand of MIS 5e (Siddall
505 et al., 2003) (Figure 8a).

506 The results of our dating, combined with existing age controls and detailed geological
507 mapping strongly supports that the observed wave-cut platforms on Cape Heraion were all
508 formed during the 125 ka highstand of MIS 5e and have been subsequently faulted since this
509 time (Figure 8c).

510

511 *4.4 Holocene displacements*

512 Offset Holocene notches and surface faulting that may be associated with the 1981
513 earthquake suggest occurrence of Holocene faulting on Cape Heraion (Figure 7). An offset
514 notch exists along the base of a cliff at the south west of the cape of as a result of slip on Fault
515 1 (Figures 4b, 7b). The highest notch is offset by 1.08 m between the footwall and the
516 hangingwall, but it does not appear that a lower notch is also offset (Figure 7b). Our
517 explanation for this is that faulting occurred on Fault 1 following the formation of the upper
518 notch between 4440-4320 B.C. (Pirazzoli et al., 1994) prior to the formation of the lowest
519 notch (at ~1.4 m) between 440-190 A.D., this may be interpreted as evidence of Holocene
520 faulting on this part of the cape.

521 Evidence of recent surface faulting may also be present on the north of the cape as a
522 several metre-deep fracture offsetting the bioherms. The fracture (Locality I Figure 4a, and
523 Figure 7d) has a strike of 245° , a horizontal offset of 43 cm, and a direction of opening of 332° ,
524 as measured by matching piercing points on both hangingwall and footwall. On Fault 17
525 between localities J and K (Figure 4a), the occurrence of surface faulting is suggested by a

526 fresh, lichen-free stripe at the base of a carbonate fault plane. These possible surface ruptures
527 were mapped over a distance of ~300 m along strike. Between localities J and K we observed
528 seven locations that display fresh lichen-free stripes on bedrock fault planes (Figure 7e and f).
529 Bedrock offsets (measured as vertical throw) appear as a light grey stripe at the base of a free
530 face, preserving what appears to be the relative coseismic movement of the colluvium along
531 the fault rupture, ranging from 3-12 cm of throw. In places, the surface rupture has also
532 stepped forward into the hangingwall, located a few centimetres to decimetres away from
533 the carbonate fault plane, to offset the hangingwall colluvial deposits (Figure 7e); vertical
534 offset in the colluvium ranges between 7-28 cm, measured at eight locations between
535 localities J and K (Figure 4a).

536 As the 1981 earthquakes are the most recent to result in surface ruptures on the Pisia
537 fault (Jackson et al. 1982; Taymaz et al., 1991; Hubert et al., 1996; Roberts, 1996a), and
538 ruptures were reported as close by as along the shore of Lake Vouliagmeni (Bornavas et al.
539 1984; Figure 2c), we suggest that it plausible that the ruptures on Cape Heraion, may have
540 also occurred coseismically during the 24th and/or 25th February 1981 earthquakes.

541

542 *4.6 Throw rates and uplift rates*

543 The absolute ages of wave-cut platforms gained in this paper constrain their formation
544 to the 125 ka highstand within MIS 5e. This means that we can quantify the throw-rate and
545 uplift-rates since 125 ka (Figure 9). To constrain the fault geometries, we used elevation data
546 for the footwall and hangingwall cut-offs along the strike of fault traces from the geological
547 and geomorphological map (Figure 4) to construct throw profiles across each fault. Plots of
548 the individual throws for all faults show that faults have maximum offset values of <40 m with
549 two faults exceeding this value (17 and 18) (Figure 9a). When all of the fault throw values and

550 rates are summed across strike they show a pattern of decreasing displacement from east to
551 west (Figure 9c). We emphasise that the data in the grey area on Figure 9c should be
552 interpreted with more caution due to the lack of absolute age control obtained for the wave-
553 cut platform located in the footwall of fault 17 (Figures 4a, 9a), but here we infer that the
554 notch and small wave-cut platform at ~92-99 m (Locality J, Figure 4a) cut into the footwall of
555 Fault 17 represents the 125 ka palaeoshoreline (Figure 8c, profile 3), and we include this in
556 our summed values.

557 When fault throw and throw rates are plotted separately for the north- and south-
558 dipping faults they mirror the pattern of summed values decreasing from east to west (Figure
559 9c). It is interesting to note that four south-dipping faults accommodate more throw
560 compared to 14 north-dipping faults with the exception between 1900-1800 m to the west of
561 the 'on fault' throw minima (Figure 9c). We postulate that this may be a reflection of the
562 broader faulting pattern within the Gulf of Corinth where the polarity of faulting switched
563 from south-dipping faults to north-dipping faults during the late Quaternary (Roberts et al.,
564 2009; Nixon et al., 2016). Specifically, Roberts et al. (2009) suggested that the north-dipping
565 SAFS experienced an increase in slip at ~175 ka. The short fault lengths and small
566 displacements of the north dipping faults on Cape Heraion may indicate that they may be less
567 mature compared to their south-dipping counterparts. As the summed throw values do not
568 decrease to zero in the mapped area, we suggest that the point of zero vertical offset may lie
569 offshore to the west of Cape Heraion, unless the faulting is actually hard-linked to offshore
570 EXFS.

571 Another way to consider the results is to explore how throw across active faults has
572 produced spatial variation in uplift relative to present-day sea-level. In other words, the
573 absolute ages of wave-cut platforms, and knowledge of their elevations, allows calculation of

574 spatial variation in uplift rates since 125 ka. Uplift rates since 125 ka from the highest and
575 lowest dated wave-cut platforms are calculated as 0.46 mm/yr (S2, 62 m) and 0.02 mm/yr
576 (Sample P1CWall, 7 m, Roberts et al., 2009) respectively (Figure 4a). If our assertion that the
577 observed notch at 92 m (Locality J, Figure 4a) marks the palaeoshoreline of the 125 ka is
578 correct then a maximum uplift rate of 0.7 mm/yr on Cape Heraion is derived using the 92 m
579 elevation (N.B. these calculations take into account that the sea-level elevation of the MIS 5e
580 highstand was +5 m relative to today's sea-level). The extreme variability in uplift rate over
581 distances of tens of metres or less precludes simple interpretations of regional tectonic signals
582 in our opinion, as the local uplift is clearly dominated by local faulting (c.f. Leeder et al. 2005).

583 While the ages obtained in this study and the existing coral U-series link the formation
584 of the wave-cut platforms to the MIS 5e highstand, field observations suggest that some faults
585 were already active prior to MIS 5e. Evidence for this is in the form of (a) marine cementation
586 within submarine scree coating the fault planes on Faults 1 and 4, (b) stratigraphic variations
587 across faults in and below the bioherms, and (c) flat-topped bioherms in the footwall versus
588 domed-topped bioherms in the hangingwall that are suggested to have grown up toward
589 water surface levels during formation (Figure 5) (also observed by Kershaw and Guo, 2006).
590 This evidence suggests that faulting on Cape Heraion was active prior to the beginning of the
591 MIS 5e (~138 ka) and continued throughout the marine stage and beyond.

592

593 **5. Discussion**

594 Detailed fault mapping and absolute dating on Cape Heraion reveals that the western
595 tip zone of the SAFS accommodates deformation via distributed faulting along synthetic and
596 antithetic faults. Importantly, our findings provide evidence of faulting during the Late
597 Quaternary, specifically over decadal, 10^3 and 10^5 year timescales that is ongoing into the

598 Holocene and perhaps even as recently as 1981. Offset marine terraces and their wave-cut
599 platforms throughout the entire mapped area can be linked to the 125 ka highstand within
600 MIS 5e. The findings presented in this study, therefore, provide evidence of significant late-
601 Quaternary faulting on Cape Heraion. This outcome is in direct contrast to the findings of
602 Leeder et al. (2003) and Leeder et al. (2005) who refute the notion of displacement of
603 Holocene and late Quaternary shoreline deposits within the study area, and conclude that the
604 Perachora Peninsula is uplifting at a constant, low, uniform rate of 0.2-0.3 mm/yr possibly
605 linked to angle of dip of the subducting African plate beneath the eastern Gulf of Corinth
606 (Leeder et al., 2005) and representing a 'background' uplift rate for the region.

607 Our fault throw analyses show that summed throw rates in the tip area appear to be
608 relatively high, up to ~1.6 mm/yr (Figure 9), compared to throw and slip rates near the centre
609 of the Pisia and Skinos faults of up to 2.3 mm/yr (Mechernich et al., 2018) and 0.7-2.5 mm/yr
610 (Collier et al., 1998) over the Holocene and 1.2-2.3 mm/yr over the longer term (Collier et al.,
611 1998). From the findings presented here, we conclude that detailed across strike mapping
612 within the tip zone of a fault is imperative in order to constrain accurate rates of long-term
613 faulting that could otherwise be underestimated. We show that the tips of faults should be
614 considered as zones of deformation, rather than localised surface features where a fault stops
615 as they contain multiple active faults.

616

617 *5.1 High throw rates on Cape Heraion*

618 Our findings lead us to question why the throw values obtained in the western tip
619 zone over 125 ka are anomalously high compared to those observed along the localised fault
620 (Figure 10a). Studies of tip displacement gradients commonly suggest high gradients occur
621 where the tips of two faults overlap, as a consequence of the interaction between the stress

622 fields of the faults (e.g. Peacock and Sanderson, 1991; Huggins et al., 1995; Willemse et al.,
623 1996; Cartwright and Mansfield, 1998; Cowie and Shipton, 1998; Gupta and Scholz, 2000;
624 Ferrill and Morris, 2001; Scholz and Lawler, 2004; Fossen and Rotevatn, 2016). Analysis of an
625 isolated fault tip by Cowie and Shipton (1998) revealed an average tip displacement gradient
626 of 0.018, whereas Cartwright and Mansfield (1998) obtained gradients between 0.0164 to
627 0.25, in their study of 20 normal faults comprised of a mixture of isolated and interacting
628 faults. In comparison, the tip displacement gradient for the investigated western tip zone of
629 the SAFS is 0.233 (Figure 10b), at the upper range of those observed above.

630 An explanation of the relatively high summed throw rates on Cape Heraion may be
631 due to fault interaction between the stress fields of the EXFS and the SAFS located along strike
632 to one another and whose eastern and western fault tips overlap (Figure 2a). While this
633 suggestion has been proposed by Morewood and Roberts, (1997), it has not been
634 quantitatively investigated. One way of exploring fault interaction between overlapping faults
635 relies on modelling the calculated Coulomb stress transfer from rupturing a source fault onto
636 a receiver fault. Studies of Coulomb stress transfer (King et al., 1994; Toda et al., 2005) show
637 that following an earthquake, changes in the stress around the slipping patch on the source
638 fault occur that may influence seismicity on neighbouring receiver faults, with positive
639 Coulomb stress transfer bringing a receiver fault closer to failure and negative Coulomb stress
640 transfer resulting in stress shadows. The presence of a stress shadow on the tip zone of a
641 receiver fault may result in deceleration of the propagation of the tip of the receiver fault,
642 which consequently results in displacement accumulating near its interacting tips, causing
643 steeper displacement gradients (Gupta and Scholz, 2000, Figure 14). The deceleration occurs
644 because the fault at the interacting tip must overcome the rupture resistance and stress drop
645 imposed by the adjacent fault (Walsh and Watterson, 1991; Scholz and Lawler, 2004).

646 We explore whether the location of the eastern EXFS tip zone (Figure 2a) could perturb
647 the stress field of the western tip zone of the SAFS by modelling the Coulomb stress changes
648 following an earthquake on the EXFS (source fault) onto the SAFS (receiver fault) using
649 Coulomb 3.3.01 software. We use the approach and updated code of Mildon et al. (2016)
650 within Coulomb 3.3.01 that allows strike-variable faults to be used, as Coulomb stress transfer
651 is particularly sensitive to changes in the strike of receiver faults (Mildon et al., 2016). An
652 accurate fault trace drawn using Google EarthTM and geometries (dip, strike, rake) of the
653 source (EXFS) and receiver (SAFS) faults (Table 4) were input into the code from Mildon et al.
654 (2016). The source fault was then ruptured to produce a 'standard' earthquake, determined
655 using fault-scaling relationships to calculate the maximum magnitude from the length of the
656 fault rupture (Wells and Coppersmith, 1994). Three source fault rupture scenarios are
657 modelled: (1) the rupture of the SAFS with the exception of the western 2.5 km of the SAFS;
658 (2) the rupture of the entire EXFS; (3) a partial rupture of the EXFS, which involves only the
659 most eastern segment (the Perachora fault) (Figure 2a). Scenario (1) was modelled in order
660 to establish the Coulomb stress transfer imparted from a partial rupture of a fault onto its
661 own tip area (e.g. Roberts 1996). Note that within the Coulomb stress transfer scenarios, the
662 western tip area of the SAFS is defined as the western 2.5 km section of the SAFS, from Point
663 A (Figure 2a) to the west tip of Cape Heraion.

664 The results of Coulomb stress transfer modelling show stress enhancement on the
665 shallow portions of faults in the region of Cape Heraion, or stress enhancement to greater
666 depths, depending on the exact source to receiver geometry. Rupturing the entire SAFS with
667 the exception of the western 2.5 km section (Scenario 1), results in a significant positive
668 Coulomb stress change of 2 bars onto the entire fault plane of the SAFS western 2.5 km
669 section (Figure 11b). Rupturing the entire EXFS (Scenario (2)) results in the upper and lower 2

670 km of the SAFS western 2.5 km section experiencing positive stress transfer of 2 bars, while
671 the majority of the western 2.5 km section of the fault plane displays negative stress transfer
672 of up to -2 bars (Figure 11c). Similarly, in scenario (3), rupturing only the Perachora fault
673 segment of the EXFS also results in negative stress transfer of -2 bars over almost all of the
674 western 2.5 km section of the fault with the exception of the upper 1 km, which experiences
675 positive stress transfer values of 1-2 bars (Figure 11d). Overall, the high values of
676 displacement observed on Cape Heraion over 125 ka may be explained by fault interaction
677 between the overlapping tips of the EXFS and the SAFS.

678

679 *5.2 Impacts on seismic hazard*

680 Our findings have implications for fault-based probabilistic seismic hazard assessment
681 (PSHA). We show here that the tip zone of a crustal-scale normal fault can accommodate
682 significant displacement 'off the localised fault', possibly linked to interaction with a
683 neighbouring fault. If these patterns of deformation are assumed to be typical for other
684 normal crustal-scale faults within fault systems that overlap along strike, such as those in the
685 Central and Southern Italian Apennines (Roberts and Michetti, 2004; Papanikolaou et al.,
686 2005; Papanikolaou and Roberts, 2007; Iezzi et al., 2019) and Basin and Range Province,
687 Western USA (e.g. Machette et al., 1991; Anders and Schlische, 1994; Schlische and Anders,
688 1996, *and references therein*) then our findings may help shed light on how to incorporate
689 slip/throw values into regional datasets, and whether displacements can jump from one
690 major fault to another.

691 It is known that measurements of slip rate are key inputs into PSHA calculations to
692 gain recurrence intervals and probability of shaking events (e.g. Boncio et al., 2004; Pace et
693 al., 2010; 2016; Valentini et al., 2017). However, due to a sparsity of data, it is common to

694 extrapolate slip rate data from measurements collected on a single location along a fault. This
695 is predominantly done by assuming that displacement decreases towards fault tips (Faure
696 walker et al., 2018). The present study shows that this approach can be problematic, because
697 the interaction between overlapping and interacting fault tips of neighbouring faults might
698 result in anomalously-high displacement in the tip zone, so that throw and slip rates do not
699 simply decrease along strike. Thus, calculation of recurrence rates and the probabilities of
700 given shaking intensities may be in error in such situations.

701 If our suggestion that high values of displacement in the overlapping tip zones
702 between the EXFS and the SAFS are as a result of fault interaction is correct, then the
703 possibility that earthquake ruptures may jump between the EXFS and SAFS should also be
704 explored. Fault interaction has the capacity to affect rupture sequences whereby seismic
705 events may 'jump' across interacting faults, causing multi-fault earthquakes (e.g. Gupta and
706 Scholz, 2000; Iezzi et al., 2019). For instance, from analysis of the source parameters of the
707 1981 earthquake sequence, Abercrombie et al. (1995) suggested that the 1981 earthquake
708 sequence might represent a multi-fault rupture between the SAFS and EXFS (or a segment of
709 the EXFS), during which the rupture might have originated offshore and propagated eastward
710 onshore. However, this analysis was carried out without consideration of the distributed
711 faulting reported herein. It is beyond the scope of this paper to confirm or deny whether the
712 presence of distributed faulting may make jumps between co-located faults more or less
713 likely. However, this topic is important because the recent UCERF 3 model (Field et al., 2017)
714 recognises the potential of ruptures to jump between faults that are co-located along strike
715 separated by small distances (5 km), a value similar to those identified by empirical studies of
716 normal faulting earthquakes between 5-7 km (e.g. DePolo et al., 1991; Wesnousky, 2008). The
717 maximum step between the SAFS and EXFS is ~4 km (Figure 2), within the values reported

718 above. Moreover, the observation that anomalously high displacement has accumulated in
719 the Cape Heraion tip zone may be evidence that earthquake ruptures do cross the tip zones,
720 but their presence is only detected if detailed mapping is conducted, and excellent age
721 constraints are available to gain rates of deformation.

722 We contrast the wealth of observations we provide in the Cape Heraion tip zone with
723 the more typical situation away from sea-level, where transverse bedrock ridges tend to
724 occupy tip zones, and these ridges are made of monotonous, uniform pre-rift lithologies with
725 sparse Quaternary or Holocene sediments to study and gain evidence for active faulting and
726 rates of deformation (e.g. Roberts and Koukouvelas, 1996, elsewhere in central Greece;
727 Roberts and Michetti, 2004, Italian Apennines; Zhang et al., 1991; Crone and Haller, 1991; Wu
728 and Bruhn, 1994 western USA, for examples of such transverse bedrock ridges). It may be that
729 displacements remain undiscovered in tip zones between major active faults, and this
730 warrants more investigation, because their study may be one of the few ways to observe
731 whether ruptures cross tip zones to produce hazardous, multi-fault earthquakes.

732

733 **6. Conclusions**

734

735 1. Cape Heraion, in the western tip zone of the South Alkyonides Fault System, deforms via a
736 set of distributed faults that are synthetic and antithetic to the 'main fault' and have been
737 active over decadal, 10^3 yr and 10^5 yr timescales. New age constraints using ^{36}Cl cosmogenic
738 exposure dating and $^{234}\text{U}/^{230}\text{Th}$ age dating of corals reinforce that the marine terraces and
739 associated wave-cut platforms on Cape Heraion are linked to the 125 ka highstand within MIS
740 5e rather than a set of terraces from three successive MIS phases.

741 2. On Cape Heraion, summed throw values (211 – 35 m), throw rates (1.68 – 0.25 mm/yr) and
742 uplift rates (maximum 0.7 mm/yr) appear to exceed those reported on the main fault. These
743 deformation rates are reflected in an anomalously high displacement gradient of 0.233.
744 Coulomb stress change modelling suggests that this is a consequence of the fault interaction
745 between the overlapping tips of the EXFS and the SAFS.

746 3. Our findings have implications for probabilistic seismic hazard calculations as they show
747 that the tip zones of crustal-scale faults may host high deformation rates caused by
748 distributed faulting and as such should be mapped in detail across strike. This is particularly
749 important for fault systems worldwide where crustal-scale faults may overlap and where the
750 slip rates are typically propagated along strike from one or two measurements assuming a
751 fault that linearly decreases to zero at the tips.

752

753 Acknowledgements

754 ³⁶Cl exposure dating was carried out by the Cosmogenic Isotope Analysis Facility (SUERC, UK)
755 via CIAF grant 9161-1015. ²³⁴U/²³⁰Th coral age dating was carried out at the Geochronology
756 and Tracers Facility (BGS, UK) via grant IP-1734-0517. We thank Athanassios Ganas and
757 Hellenic Cadastre SA for DEM data via and sincere thanks to Christina Tsimi (NOA) for
758 customising the 5 m digital elevation models for the research area. We also thank Zoe Mildon
759 for sharing her modified Coulomb code and providing support to us when modelling. This
760 study has benefited from discussions with Rebecca Bell, Imperial College, London.

761

762 Abercrombie, R. E., Main, I. G., Douglas, A., & Burton, P. W. (1995). The nucleation and
763 rupture process of the 1981 Gulf of Corinth earthquakes from deconvolved broad-band
764 data. *Geophysical Journal International*, 120(2), 393-405.

- 765 Anders, M. H., & Schlische, R. W. (1994). Overlapping faults, intrabasin highs, and the
766 growth of normal faults. *The Journal of Geology*, 102(2), 165-179.
- 767 Andrews, J. E., Leeder, M. R., Portman, C., Rowe, P. J., Smith, J., Kershaw, S., & Guo, L.
768 (2007). Discussion on Pleistocene calcified cyanobacterial mounds, Perachora peninsula,
769 central Greece: a controversy of growth and history Geological Society, London, Special
770 Publications, Vol. 255, 2006, 53–69. *Journal of the Geological Society*, 164(5), 1065-1072.
- 771 Armijo, R., Lyon-Caen, H., & Papanastassiou, D. (1991). A possible normal-fault rupture for
772 the 464 BC Sparta earthquake. *Nature*, 351(6322), 137.
- 773
774 Armijo, R., Meyer, B. G. C. P., King, G. C. P., Rigo, A., & Papanastassiou, D. (1996).
775 Quaternary evolution of the Corinth Rift and its implications for the Late Cenozoic evolution
776 of the Aegean. *Geophysical Journal International*, 126(1), 11-53.
- 777 Bell, R. E., McNeill, L. C., Bull, J. M., Henstock, T. J., Collier, R. L., & Leeder, M. R. (2009). Fault
778 architecture, basin structure and evolution of the Gulf of Corinth Rift, central Greece. *Basin
779 Research*, 21(6), 824-855.
- 780 Binnie, A., Dunai, T. J., Binnie, S. A., Victor, P., González, G., & Bolten, A. (2016). Accelerated
781 late quaternary uplift revealed by ¹⁰Be exposure dating of marine terraces, Mejillones
782 Peninsula, northern Chile. *Quaternary Geochronology*, 36, 12-27.
- 783 Boncio, P., Lavecchia, G., & Pace, B. (2004). Defining a model of 3D seismogenic sources for
784 Seismic Hazard Assessment applications: the case of central Apennines (Italy). *Journal of
785 Seismology*, 8(3), 407-425.
- 786 Bornovas, J., Gaitanakis, P., & Spiridopoulos, A. (1984). *Geological map of Greece, 1:50,000,
787 Perachora Sheet*. Athens: IGME.
- 788 Boulton, S. J., & Stewart, I. S. (2015). Holocene coastal notches in the Mediterranean region:
789 Indicators of palaeoseismic clustering?. *Geomorphology*, 237, 29-37.
- 790 Briole, P., Rigo, A., Lyon-Caen, H., Ruegg, J. C., Papazissi, K., Mitsakaki, C., ... & Deschamps,
791 A. (2000). Active deformation of the Corinth rift, Greece: results from repeated Global
792 Positioning System surveys between 1990 and 1995. *Journal of Geophysical Research: Solid
793 Earth*, 105(B11), 25605-25625.
- 794 Cartwright, J. A., & Mansfield, C. S. (1998). Lateral displacement variation and lateral tip
795 geometry of normal faults in the Canyonlands National Park, Utah. *Journal of Structural
796 Geology*, 20(1), 3-19.
- 797 Charalampakis, M., Lykousis, V., Sakellariou, D., Papatheodorou, G., & Ferentinos, G. (2014).
798 The tectono-sedimentary evolution of the Lechaion Gulf, the south eastern branch of the
799 Corinth graben, Greece. *Marine Geology*, 351, 58-75.

- 800 Cheng, H., Edwards, R. L., Shen, C. C., Polyak, V. J., Asmerom, Y., Woodhead, J., ... & Wang,
801 X. (2013). Improvements in ^{230}Th dating, ^{230}Th and ^{234}U half-life values, and U–Th
802 isotopic measurements by multi-collector inductively coupled plasma mass spectrometry.
803 *Earth and Planetary Science Letters*, 371, 82-91.
- 804 Clarke, P. J., Davies, R. R., England, P. C., Parsons, B., Billiris, H., Paradissis, D., ... & Bingley, R.
805 (1998). Crustal strain in central Greece from repeated GPS measurements in the interval
806 1989–1997. *Geophysical Journal International*, 135(1), 195-214.
- 807 Collier, R. L., Leeder, M. R., Rowe, P. J., & Atkinson, T. C. (1992). Rates of tectonic uplift in
808 the Corinth and Megara basins, central Greece. *Tectonics*, 11(6), 1159-1167.
- 809 Collier, R. E., Leeder, M. R., Trout, M., Ferentinos, G., Lyberis, E., & Papatheodorou, G.
810 (2000). High sediment yields and cool, wet winters: Test of last glacial paleoclimates in the
811 northern Mediterranean. *Geology*, 28(11), 999-1002.
- 812 Collier, R. E., Pantosti, D., D'addezio, G., De Martini, P. M., Masana, E., & Sakellariou, D.
813 (1998). Paleoseismicity of the 1981 Corinth earthquake fault: Seismic contribution to
814 extensional strain in central Greece and implications for seismic hazard. *Journal of*
815 *Geophysical Research: Solid Earth*, 103(B12), 30001-30019.
- 816 Cooper, F. J., Roberts, G. P., & Underwood, C. J. (2007). A comparison of 103–105 year uplift
817 rates on the South Alkyonides Fault, central Greece: Holocene climate stability and the
818 formation of coastal notches. *Geophysical Research Letters*, 34(14).
- 819 Cowie, P. A., & Roberts, G. P. (2001). Constraining slip rates and spacings for active normal
820 faults. *Journal of Structural Geology*, 23(12), 1901-1915.
- 821 Cowie, P. A., & Shipton, Z. K. (1998). Fault tip displacement gradients and process zone
822 dimensions. *Journal of Structural Geology*, 20(8), 983-997.
- 823 Crémière, A., Lepland, A., Chand, S., Sahy, D., Condon, D. J., Noble, S. R., ... & Brunstad, H.
824 (2016). Timescales of methane seepage on the Norwegian margin following collapse of the
825 Scandinavian Ice Sheet. *Nature communications*, 7, 11509.
- 826 Crone, A. J., & Haller, K. M. (1991). Segmentation and the coseismic behavior of Basin and
827 Range normal faults: examples from east-central Idaho and southwestern Montana, USA.
828 *Journal of Structural Geology*, 13(2), 151-164.
- 829 Davies, R., England, P. C., Parsons, B., Billiris, H., Paradissis, D., & Veis, G. (1997). Geodetic
830 strain of Greece in the interval 1892–1992. *Journal of Geophysical Research: Solid Earth*,
831 102(B11), 24571-24588.
- 832 DePolo, C. M., Clark, D. G., Slemmons, D. B., & Ramelli, A. R. (1991). Historical surface
833 faulting in the Basin and Range province, western North America: implications for fault
834 segmentation. *Journal of structural Geology*, 13(2), 123-136.

- 835 Devescovi, M., & Iveša, L. (2008). Colonization patterns of the date mussel *Lithophaga*
836 *lithophaga* (L., 1758) on limestone breakwater boulders of a marina. *Periodicum biologorum*,
837 *110*(4), 339-345.
- 838 Dia, A. N., Cohen, A. S., O'nions, R. K., & Jackson, J. A. (1997). Rates of uplift investigated
839 through ²³⁰Th dating in the Gulf of Corinth (Greece). *Chemical Geology*, *138*(3-4), 171-184.
- 840 Dunai, T. (2010). *Cosmogenic nuclides, principles, concepts and applications in the Earth*
841 *surface sciences*. Cambridge: Cambridge University Press
- 842 Dutton, A., Carlson, A. E., Long, A., Milne, G. A., Clark, P. U., DeConto, R., ... & Raymo, M. E.
843 (2015). Sea-level rise due to polar ice-sheet mass loss during past warm periods. *science*,
844 *349*(6244), aaa4019.
- 845 Dutton, A., & Lambeck, K. (2012). Ice volume and sea level during the last interglacial.
846 *science*, *337*(6091), 216-219.
- 847 Faure Walker, J. P., Visini, F., Roberts, G., Galasso, C., McCaffrey, K., & Mildon, Z. (2018).
848 Variable Fault Geometry Suggests Detailed Fault-Slip-Rate Profiles and Geometries Are
849 Needed for Fault-Based Probabilistic Seismic Hazard Assessment (PSHA). *Bulletin of the*
850 *Seismological Society of America*, *109*(1), 110-123.
- 851 Fernández-Blanco, D., de Gelder, G., Lacassin, R., & Armijo, R. (2019). A new crustal fault
852 formed the modern Corinth Rift. *Earth-Science Reviews*, 102919.
- 853 Ferrill, D. A., & Morris, A. P. (2001). Displacement gradient and deformation in normal fault
854 systems. *Journal of Structural Geology*, *23*(4), 619-638.
- 855 Field, E. H., Arrowsmith, R. J., Biasi, G. P., Bird, P., Dawson, T. E., Felzer, K. R., ... & Michael,
856 A. J. (2014). Uniform California earthquake rupture forecast, version 3 (UCERF3)—The time-
857 independent model. *Bulletin of the Seismological Society of America*, *104*(3), 1122-1180.
- 858 Field, E. H., Milner, K. R., Hardebeck, J. L., Page, M. T., van der Elst, N., Jordan, T. H., ... &
859 Werner, M. J. (2017). A spatiotemporal clustering model for the third Uniform California
860 Earthquake Rupture Forecast (UCERF3-ETAS): Toward an operational earthquake forecast.
861 *Bulletin of the Seismological Society of America*, *107*(3), 1049-1081.
- 862 Fossen, H., & Rotevatn, A. (2016). Fault linkage and relay structures in extensional settings—
863 A review. *Earth-Science Reviews*, *154*, 14-28.
- 864 Gallen, S. F., Wegmann, K. W., Bohnenstiehl, D. R., Pazzaglia, F. J., Brandon, M. T., &
865 Fassoulas, C. (2014). Active simultaneous uplift and margin-normal extension in a forearc
866 high, Crete, Greece. *Earth and Planetary Science Letters*, *398*, 11-24.
- 867 Galli, P., Galadini, F., & Pantosti, D. (2008). Twenty years of paleoseismology in Italy. *Earth-*
868 *Science Reviews*, *88*(1-2), 89-117.

- 869 Gallup, C. D., Cheng, H., Taylor, F. W., & Edwards, R. L. (2002). Direct determination of the
870 timing of sea level change during Termination II. *Science*, 295(5553), 310-313.
- 871 Grant, K. M., Rohling, E. J., Ramsey, C. B., Cheng, H., Edwards, R. L., Florindo, F., ... &
872 Williams, F. (2014). Sea-level variability over five glacial cycles. *Nature communications*, 5,
873 5076.
- 874 Griggs, G. B., Trenhaile, A. S., Carter, R. W. G., & Woodroffe, C. D. (1994). *Coastal cliffs and*
875 *platforms* (pp. 425-450). Cambridge University Press, Cambridge, UK.
- 876 Gupta, A., & Scholz, C. H. (2000). A model of normal fault interaction based on observations
877 and theory. *Journal of Structural Geology*, 22(7), 865-879.
- 878 Hearty, P. J., Hollin, J. T., Neumann, A. C., O'Leary, M. J., & McCulloch, M. (2007). Global sea-
879 level fluctuations during the Last Interglaciation (MIS 5e). *Quaternary Science Reviews*,
880 26(17-18), 2090-2112.
- 881 Houghton, 2010. Unpublished Thesis. Birkbeck College, University of London.
- 882 Hubert, A., King, G., Armijo, R., Meyer, B., & Papanastasiou, D. (1996). Fault re-activation,
883 stress interaction and rupture propagation of the 1981 Corinth earthquake sequence. *Earth*
884 *and Planetary Science Letters*, 142(3-4), 573-585.
- 885 Huggins, P., Watterson, J., Walsh, J. J., & Childs, C. (1995). Relay zone geometry and
886 displacement transfer between normal faults recorded in coal-mine plans. *Journal of*
887 *Structural Geology*, 17(12), 1741-1755.
- 888 Iezzi, F., Mildon, Z., Walker, J. F., Roberts, G., Goodall, H., Wilkinson, M., & Robertson, J.
889 (2018). Coseismic throw variation across along-strike bends on active normal faults:
890 Implications for displacement versus length scaling of earthquake ruptures. *Journal of*
891 *Geophysical Research: Solid Earth*, 123(11), 9817-9841.
- 892 Iezzi, F., Roberts, G., Walker, J. F., & Papanikolaou, I. (2019). Occurrence of partial and total
893 coseismic ruptures of segmented normal fault systems: Insights from the Central Apennines,
894 Italy. *Journal of Structural Geology*, 126, 83-99.
- 895 Jackson, J. A., Gagnepain, J., Houseman, G., King, G. C. P., Papadimitriou, P., Soufleris, C., &
896 Virieux, J. (1982). Seismicity, normal faulting, and the geomorphological development of the
897 Gulf of Corinth (Greece): the Corinth earthquakes of February and March 1981. *Earth and*
898 *Planetary Science Letters*, 57(2), 377-397.
- 899 Jara-Muñoz, J., Melnick, D., Zambrano, P., Rietbrock, A., González, J., Argandoña, B., &
900 Strecker, M. R. (2017). Quantifying offshore fore-arc deformation and splay-fault slip using
901 drowned Pleistocene shorelines, Arauco Bay, Chile. *Journal of Geophysical Research: Solid*
902 *Earth*, 122(6), 4529-4558.

- 903 Kershaw, S., & Guo, L. (2001). Marine notches in coastal cliffs: indicators of relative sea-level
904 change, Perachora Peninsula, central Greece. *Marine Geology*, 179(3-4), 213-228.
- 905 Kershaw, S., & Guo, L. (2003). Pleistocene cyanobacterial mounds in the Perachora
906 Peninsula, Gulf of Corinth, Greece: structure and applications to interpreting sea-level
907 history and terrace sequences in an unstable tectonic setting. *Palaeogeography,*
908 *Palaeoclimatology, Palaeoecology*, 193(3-4), 503-514.
- 909 Kershaw, S., & Guo, L. (2006). Pleistocene calcified cyanobacterial mounds, Perachora
910 Peninsula, central Greece: a controversy of growth and history. *Geological Society, London,*
911 *Special Publications*, 255(1), 53-69.
- 912 King, G. C., Stein, R. S., & Lin, J. (1994). Static stress changes and the triggering of
913 earthquakes. *Bulletin of the Seismological Society of America*, 84(3), 935-953.
- 914 Kopp, R. E., Simons, F. J., Mitrovica, J. X., Maloof, A. C., & Oppenheimer, M. (2009).
915 Probabilistic assessment of sea level during the last interglacial stage. *Nature*, 462(7275),
916 863.
- 917 Lajoie, K. R. (1986). Coastal tectonics. *Active tectonics*, 95-124.
- 918 Lambeck, K., Esat, T. M., & Potter, E. K. (2002). Links between climate and sea levels for the
919 past three million years. *Nature*, 419(6903), 199.
- 920 Leeder, M. R., McNeill, L. C., LI Collier, R. E., Portman, C., Rowe, P. J., Andrews, J. E., &
921 Gawthorpe, R. L. (2003). Corinth rift margin uplift: New evidence from Late Quaternary
922 marine shorelines. *Geophysical Research Letters*, 30(12).
- 923 Leeder, M. R., Portman, C., Andrews, J. E., Collier, R. L., Finch, E., Gawthorpe, R. L., ... &
924 Rowe, P. (2005). Normal faulting and crustal deformation, Alkyonides Gulf and Perachora
925 peninsula, eastern Gulf of Corinth rift, Greece. *Journal of the Geological Society*, 162(3), 549-
926 561.
- 927 Leeder, M. R., Seger, M. J., & Stark, C. P. (1991). Sedimentation and tectonic geomorphology
928 adjacent to major active and inactive normal faults, southern Greece. *Journal of the*
929 *Geological Society*, 148(2), 331-343.
- 930 Licciardi, J. M., Denoncourt, C. L., & Finkel, R. C. (2008). Cosmogenic ³⁶Cl production rates
931 from Ca spallation in Iceland. *Earth and Planetary Science Letters*, 267(1-2), 365-377.
- 932 Machette, M. N., Personius, S. F., Nelson, A. R., Schwartz, D. P., & Lund, W. R. (1991). The
933 Wasatch fault zone, Utah—Segmentation and history of Holocene earthquakes. *Journal of*
934 *Structural Geology*, 13(2), 137-149.
- 935 Marrero, S. M., Phillips, F. M., Caffee, M. W., & Gosse, J. C. (2016). CRONUS-Earth
936 cosmogenic ³⁶Cl calibration. *Quaternary Geochronology*, 31, 199-219.

- 937 McGrath, A. G., & Davison, I. (1995). Damage zone geometry around fault tips. *Journal of*
938 *Structural Geology*, 17(7), 1011-1024.
- 939 McLeod, A. E., Dawers, N. H., & Underhill, J. R. (2000). The propagation and linkage of
940 normal faults: insights from the Strathspey–Brent–Statfjord fault array, northern North Sea.
941 *Basin Research*, 12(3-4), 263-284.
- 942 McNeill, L. C., & Collier, R. L. (2004). Uplift and slip rates of the eastern Eliki fault segment,
943 Gulf of Corinth, Greece, inferred from Holocene and Pleistocene terraces. *Journal of the*
944 *Geological Society*, 161(1), 81-92.
- 945 McNeill, L. C., Cotterill, C. J., Henstock, T. J., Bull, J. M., Stefatos, A., Collier, R. L., ... & Hicks,
946 S. E. (2005). Active faulting within the offshore western Gulf of Corinth, Greece: Implications
947 for models of continental rift deformation. *Geology*, 33(4), 241-244.
- 948 Mechernich, S., Schneiderwind, S., Mason, J., Papanikolaou, I. D., Deligiannakis, G.,
949 Pallikarakis, A., ... & Reicherter, K. (2018). The seismic history of the Pisias fault (eastern
950 Corinth rift, Greece) from fault plane weathering features and cosmogenic ³⁶Cl dating.
951 *Journal of Geophysical Research: Solid Earth*, 123(5), 4266-4284.
- 952 Meschis, M., Roberts, G. P., Robertson, J., & Briant, R. M. (2018). The Relationships Between
953 Regional Quaternary Uplift, Deformation Across Active Normal Faults, and Historical
954 Seismicity in the Upper Plate of Subduction Zones: The Capo D'Orlando Fault, NE Sicily.
955 *Tectonics*, 37(5), 1231-1255.
- 956 Mildon, Z. K., Toda, S., Faure Walker, J. P., & Roberts, G. P. (2016a). Evaluating models of
957 Coulomb stress transfer: Is variable fault geometry important?. *Geophysical Research*
958 *Letters*, 43(24).
- 959 Miller, W. R., & Mason, T. R. (1994). Erosional features of coastal beachrock and aeolianite
960 outcrops in Natal and Zululand, South Africa. *Journal of Coastal Research*, 374-394.
- 961 Moretti, I., Sakellariou, D., Lykousis, V., & Micarelli, L. (2003). The Gulf of Corinth: an active
962 half graben?. *Journal of Geodynamics*, 36(1-2), 323-340.
- 963 Morewood, N. C., & Roberts, G. P. (1997). Geometry, kinematics and rates of deformation in
964 a normal fault segment boundary, central Greece. *Geophysical Research Letters*, 24(23),
965 3081-3084.
- 966 Morewood, N. C., & Roberts, G. P. (1999). Lateral propagation of the surface trace of the
967 South Alkyonides normal fault segment, central Greece: its impact on models of fault
968 growth and displacement–length relationships. *Journal of Structural Geology*, 21(6), 635-
969 652.
- 970 Morewood, N. C., & Roberts, G. P. (2001). Comparison of surface slip and focal mechanism
971 slip data along normal faults: an example from the eastern Gulf of Corinth, Greece. *Journal*
972 *of Structural Geology*, 23(2-3), 473-487.

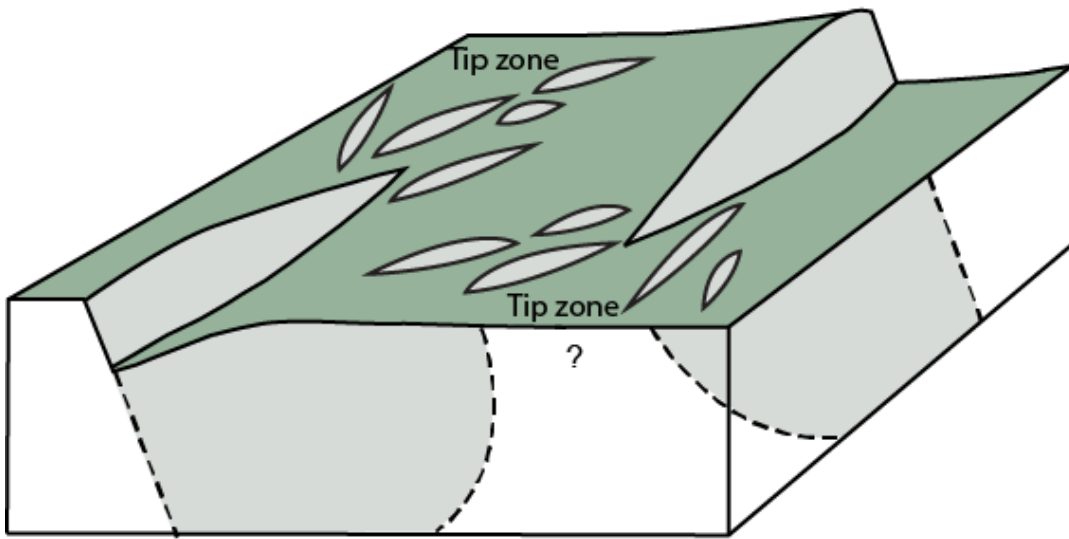
- 973 Morewood, N. C., & Roberts, G. P. (2002). Surface observations of active normal fault
974 propagation: implications for growth. *Journal of the Geological Society*, 159(3), 263-272.
- 975 Mozafari, N., SÜMER, Ö., Tikhomirov, D., Ivy-Ochs, S., Alfimov, V., Vockenhuber, C., ... &
976 Akcar, N. (2019). Holocene seismic activity of the Priene-Sazlı Fault revealed by cosmogenic
977 ³⁶Cl, Western Anatolia, Turkey 2. *Turkish Journal of Earth Sciences*, 28(3).
- 978 Muhs, D. R., & Szabo, B. J. (1994). New uranium-series ages of the Waimanalo Limestone,
979 Oahu, Hawaii: implications for sea level during the last interglacial period. *Marine Geology*,
980 118(3-4), 315-326.
- 981 Nixon, C. W., McNeill, L. C., Bull, J. M., Bell, R. E., Gawthorpe, R. L., Henstock, T. J., ... &
982 Ferentinos, G. (2016). Rapid spatiotemporal variations in rift structure during development
983 of the Corinth Rift, central Greece. *Tectonics*, 35(5), 1225-1248.
- 984 O'Leary, M. J., Hearty, P. J., Thompson, W. G., Raymo, M. E., Mitrovica, J. X., & Webster, J.
985 M. (2013). Ice sheet collapse following a prolonged period of stable sea level during the last
986 interglacial. *Nature Geoscience*, 6(9), 796.
- 987 Pace, B., Peruzza, L., Lavecchia, G., & Boncio, P. (2006). Layered seismogenic source model
988 and probabilistic seismic-hazard analyses in central Italy. *Bulletin of the Seismological
989 Society of America*, 96(1), 107-132.
- 990 Pace, B., Peruzza, L., & Visini, F. (2010). LASSCI2009. 2: layered earthquake rupture forecast
991 model for central Italy, submitted to the CSEP project. *Annals of Geophysics*.
- 992 Pace, B., Visini, F., & Peruzza, L. (2016). FiSH: MATLAB tools to turn fault data into seismic-
993 hazard models. *Seismological Research Letters*, 87(2A), 374-386.
- 994 Papanikolaou, I. D., & Roberts, G. P. (2007). Geometry, kinematics and deformation rates
995 along the active normal fault system in the southern Apennines: Implications for fault
996 growth. *Journal of Structural Geology*, 29(1), 166-188.
- 997 Papanikolaou, I. D., Roberts, G. P., & Michetti, A. M. (2005). Fault scarps and deformation
998 rates in Lazio–Abruzzo, Central Italy: Comparison between geological fault slip-rate and GPS
999 data. *Tectonophysics*, 408(1-4), 147-176.
- 1000 Peacock, D. C. P. (2002). Propagation, interaction and linkage in normal fault systems. *Earth-
1001 Science Reviews*, 58(1-2), 121-142.
- 1002 Peacock, D. C. P., & Sanderson, D. J. (1991). Displacements, segment linkage and relay
1003 ramps in normal fault zones. *Journal of Structural Geology*, 13(6), 721-733.
- 1004 Peacock, D. C. P., & Sanderson, D. J. (1994). Geometry and development of relay ramps in
1005 normal fault systems. *AAPG bulletin*, 78(2), 147-165.

- 1006 Peharda, M., Puljas, S., Chauvaud, L., Schöne, B. R., Ezgeta-Balić, D., & Thébault, J. (2015).
1007 Growth and longevity of *Lithophaga lithophaga*: what can we learn from shell structure and
1008 stable isotope composition?. *Marine biology*, 162(8), 1531-1540.
- 1009 Perrin, C., Manighetti, I., & Gaudemer, Y. (2016). Off-fault tip splay networks: A genetic and
1010 generic property of faults indicative of their long-term propagation. *Comptes Rendus*
1011 *Geoscience*, 348(1), 52-60.
- 1012 Pirazzoli, P. A. (1986). Marine notches. In *Sea-Level Research* (pp. 361-400). Springer,
1013 Dordrecht.
- 1014 Pirazzoli, P. A., Stiros, S. C., Arnold, M., Laborel, J., Laborel-Deguen, F., & Papageorgiou, S.
1015 (1994). Episodic uplift deduced from Holocene shorelines in the Perachora Peninsula,
1016 Corinth area, Greece. *Tectonophysics*, 229(3-4), 201-209.
- 1017 Portman, C., Andrews, J. E., Rowe, P. J., Leeder, M. R., & Hoogewerff, J. (2005). Submarine-
1018 spring controlled calcification and growth of large *Rivularia* bioherms, Late Pleistocene (MIS
1019 5e), Gulf of Corinth, Greece. *Sedimentology*, 52(3), 441-465.
- 1020 Richter, D. K., & Sedat, R. (1983). Brackish-water oncoids composed of blue-green and red
1021 algae from a Pleistocene terrace near Corinth, Greece. In *Coated grains* (pp. 299-307).
1022 Springer, Berlin, Heidelberg.
- 1023 Roberts, G. P. (1996a). Noncharacteristic normal faulting surface ruptures from the Gulf of
1024 Corinth, Greece. *Journal of Geophysical Research: Solid Earth*, 101(B11), 25255-25267.
- 1025 Roberts, G. P. (1996b). Variation in fault-slip directions along active and segmented normal
1026 fault systems. *Journal of Structural Geology*, 18(6), 835-845.
- 1027 Roberts, G. P., & Koukouvelas, I. (1996). Structural and seismological segmentation of the
1028 Gulf of Corinth fault system: implications for models of fault growth.
- 1029 Roberts, G. P., Houghton, S. L., Underwood, C., Papanikolaou, I., Cowie, P. A., van Calsteren,
1030 P., ... & McArthur, J. M. (2009). Localization of Quaternary slip rates in an active rift in 105
1031 years: An example from central Greece constrained by 234U-230Th coral dates from uplifted
1032 paleoshorelines. *Journal of Geophysical Research: Solid Earth*, 114(B10).
- 1033 Roberts, G. P., Meschis, M., Houghton, S., Underwood, C., & Briant, R. M. (2013). The
1034 implications of revised Quaternary palaeoshoreline chronologies for the rates of active
1035 extension and uplift in the upper plate of subduction zones. *Quaternary Science Reviews*, 78,
1036 169-187.
- 1037 Roberts, G. P., & Michetti, A. M. (2004). Spatial and temporal variations in growth rates
1038 along active normal fault systems: an example from The Lazio–Abruzzo Apennines, central
1039 Italy. *Journal of Structural Geology*, 26(2), 339-376.

- 1040 Roberts, S., & Jackson, J. (1991). Active normal faulting in central Greece: an overview.
1041 *Geological Society, London, Special Publications*, 56(1), 125-142.
- 1042 Robertson, J., Meschis, M., Roberts, G. P., Ganas, A., & Gheorghiu, D. (2019). Temporally
1043 constant Quaternary uplift rates and their relationship with extensional upper-plate faults in
1044 south Crete (Greece), constrained with ³⁶Cl cosmogenic exposure dating. *Tectonics*.
- 1045 Sachpazi, M., Clément, C., Laigle, M., Hirn, A., & Roussos, N. (2003). Rift structure, evolution,
1046 and earthquakes in the Gulf of Corinth, from reflection seismic images. *Earth and Planetary
1047 Science Letters*, 216(3), 243-257.
- 1048 Sakellariou, D., Lykousis, V., Alexandri, S., Kaberi, H., Rousakis, G., Nomikou, P., ... & Ballas,
1049 D. (2007). Faulting, seismic-stratigraphic architecture and late quaternary evolution of the
1050 Gulf of Alkyonides Basin-East Gulf of Corinth, Central Greece. *Basin Research*, 19(2), 273-
1051 295.
- 1052 Schimmelpfennig, I., Benedetti, L., Finkel, R., Pik, R., Blard, P. H., Bourles, D., ... & Williams,
1053 A. (2009). Sources of in-situ ³⁶Cl in basaltic rocks. Implications for calibration of production
1054 rates. *Quaternary Geochronology*, 4(6), 441-461.
- 1055 Schlagenhauf, A., Gaudemer, Y., Benedetti, L., Manighetti, I., Palumbo, L., Schimmelpfennig,
1056 I., ... & Pou, K. (2010). Using in situ Chlorine-36 cosmonuclide to recover past earthquake
1057 histories on limestone normal fault scarps: a reappraisal of methodology and
1058 interpretations. *Geophysical Journal International*, 182(1), 36-72.
- 1059 Schlische, R. W., & Anders, M. H. (1996). Stratigraphic effects and tectonic implications of
1060 the growth of normal faults and extensional basins. *Special Papers-Geological Society of
1061 America*, 183-203.
- 1062 Schlische, R. W., Young, S. S., Ackermann, R. V., & Gupta, A. (1996). Geometry and scaling
1063 relations of a population of very small rift-related normal faults. *Geology*, 24(8), 683-686.
- 1064 Schneiderwind, S., Boulton, S. J., Papanikolaou, I., Kázmér, M., & Reicherter, K. (2017a).
1065 Numerical modeling of tidal notch sequences on rocky coasts of the Mediterranean Basin.
1066 *Journal of Geophysical Research: Earth Surface*, 122(5), 1154-1181.
- 1067 Schneiderwind, S., Boulton, S. J., Papanikolaou, I., & Reicherter, K. (2017b). Innovative tidal
1068 notch detection using TLS and fuzzy logic: Implications for palaeo-shorelines from
1069 compressional (Crete) and extensional (Gulf of Corinth) tectonic settings. *Geomorphology*,
1070 283, 189-200.
- 1071 Scholz, C. H., & Gupta, A. (2000). Fault interactions and seismic hazard. *Journal of
1072 Geodynamics*, 29(3-5), 459-467.
- 1073 Scholz, C. H., & Lawler, T. M. (2004). Slip tapers at the tips of faults and earthquake
1074 ruptures. *Geophysical research letters*, 31(21).

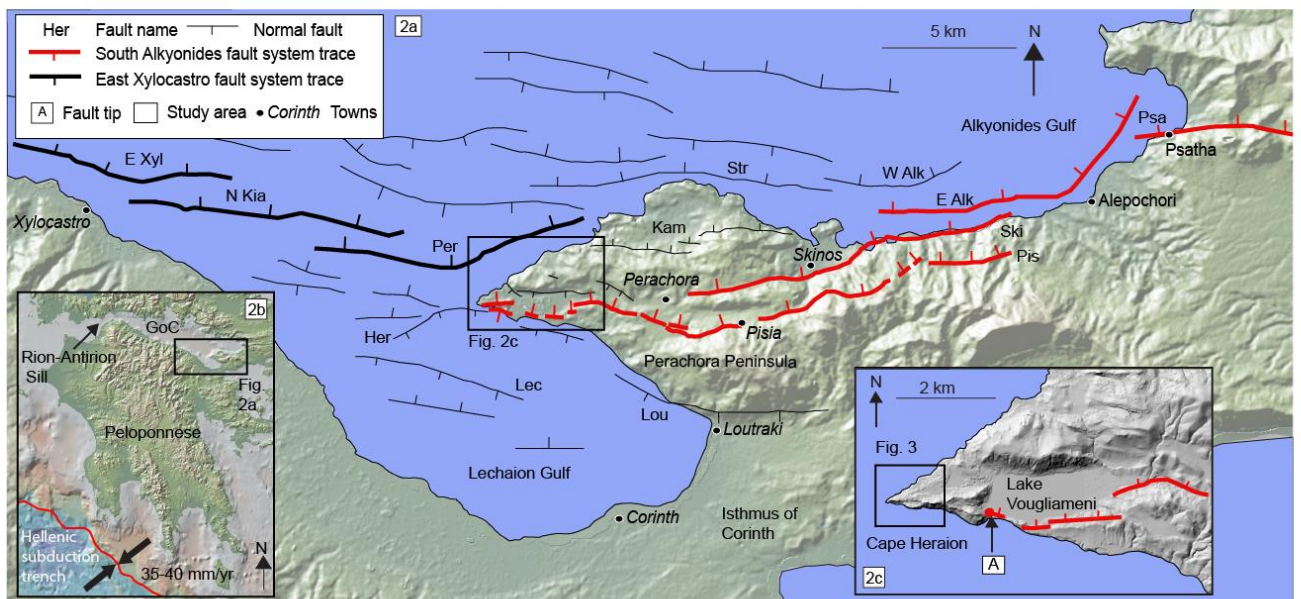
- 1075 Scott, A (1995). Unpublished Thesis, University of Manchester
- 1076 Siddall, M., Rohling, E. J., Almogi-Labin, A., Hemleben, C., Meischner, D., Schmelzer, I., &
1077 Smeed, D. A. (2003). Sea-level fluctuations during the last glacial cycle. *Nature*, 423(6942),
1078 853.
- 1079 Sieh, K., Stuiver, M., & Brillinger, D. (1989). A more precise chronology of earthquakes
1080 produced by the San Andreas fault in southern California. *Journal of Geophysical Research:*
1081 *Solid Earth*, 94(B1), 603-623.
- 1082 Spratt, R. M., & Lisiecki, L. E. (2016). A Late Pleistocene sea level stack. *Climate of the Past*,
1083 12(4), 1079-1092.
- 1084
- 1085 Stefatos, A., Papatheodorou, G., Ferentinos, G., Leeder, M., & Collier, R. (2002). Seismic
1086 reflection imaging of active offshore faults in the Gulf of Corinth: their seismotectonic
1087 significance. *Basin Research*, 14(4), 487-502.
- 1088 Stirling, C. H., & Andersen, M. B. (2009). Uranium-series dating of fossil coral reefs:
1089 extending the sea-level record beyond the last glacial cycle. *Earth and Planetary Science*
1090 *Letters*, 284(3-4), 269-283.
- 1091 Stirling, C. H., Esat, T. M., Lambeck, K., & McCulloch, M. T. (1998). Timing and duration of
1092 the Last Interglacial: evidence for a restricted interval of widespread coral reef growth.
1093 *Earth and Planetary Science Letters*, 160(3-4), 745-762.
- 1094 Stiros, S. C., & Pirazzoli, P. A. (1995). Palaeoseismic studies in Greece: a review. *Quaternary*
1095 *International*, 25, 57-63.
- 1096 Stone, J., Lambeck, K., Fifield, L. K., Evans, J. T., & Cresswell, R. G. (1996). A lateglacial age for
1097 the main rock platform, western Scotland. *Geology*, 24(8), 707-710.
- 1098 Taylor, B., Weiss, J. R., Goodliffe, A. M., Sachpazi, M., Laigle, M., & Hirn, A. (2011). The
1099 structures, stratigraphy and evolution of the Gulf of Corinth rift, Greece. *Geophysical Journal*
1100 *International*, 185(3), 1189-1219.
- 1101 Taymaz, T., Jackson, J., & McKenzie, D. (1991). Active tectonics of the north and central
1102 Aegean Sea. *Geophysical Journal International*, 106(2), 433-490.
- 1103 Toda, S., Stein, R. S., Richards-Dinger, K., & Bozkurt, S. B. (2005). Forecasting the evolution of
1104 seismicity in southern California: Animations built on earthquake stress transfer. *Journal of*
1105 *Geophysical Research: Solid Earth*, 110(B5).
- 1106 Valentini, A., Visini, F., & Pace, B. (2017). Integrating faults and past earthquakes into a
1107 probabilistic seismic hazard model for peninsular Italy. *Natural Hazards Earth System*
1108 *Sciences*.

- 1109 Vita-Finzi, C. (1993). Evaluating late Quaternary uplift in Greece and Cyprus. *Geological*
1110 *Society, London, Special Publications*, 76(1), 417-424.
- 1111 Waelbroeck, C., Labeyrie, L., Michel, E., Duplessy, J. C., McManus, J. F., Lambeck, K., ... &
1112 Labracherie, M. (2002). Sea-level and deep water temperature changes derived from
1113 benthic foraminifera isotopic records. *Quaternary Science Reviews*, 21(1-3), 295-305.
- 1114 Wells, D. L., & Coppersmith, K. J. (1994). New empirical relationships among magnitude,
1115 rupture length, rupture width, rupture area, and surface displacement. *Bulletin of the*
1116 *seismological Society of America*, 84(4), 974-1002.
- 1117 Wesnousky, S. G. (2008). Displacement and geometrical characteristics of earthquake
1118 surface ruptures: Issues and implications for seismic-hazard analysis and the process of
1119 earthquake rupture. *Bulletin of the Seismological Society of America*, 98(4), 1609-1632.
- 1120 Wesnousky, S. G., & Biasi, G. P. (2011). The length to which an earthquake will go to rupture.
1121 *Bulletin of the Seismological Society of America*, 101(4), 1948-1950.
- 1122 Westaway, R. (1993). Quaternary uplift of southern Italy. *Journal of Geophysical Research:*
1123 *Solid Earth*, 98(B12), 21741-21772.
- 1124 Wu, D., & Bruhn, R. L. (1994). Geometry and kinematics of active normal faults, South
1125 Oquirrh Mountains, Utah: implication for fault growth. *Journal of Structural Geology*, 16(8),
1126 1061-1075.
- 1127 Willemse, E. J., Pollard, D. D., & Aydin, A. (1996). Three-dimensional analyses of slip
1128 distributions on normal fault arrays with consequences for fault scaling. *Journal of Structural*
1129 *Geology*, 18(2-3), 295-309.
- 1130 Yielding, G., Needham, T., & Jones, H. (1996). Sampling of fault populations using sub-
1131 surface data: a review. *Journal of Structural Geology*, 18(2-3), 135-146.
- 1132 Zhang, P., Slemmons, D. B., & Mao, F. (1991). Geometric pattern, rupture termination and
1133 fault segmentation of the Dixie Valley—Pleasant Valley active normal fault system, Nevada,
1134 USA. *Journal of Structural Geology*, 13(2), 165-176.



1135

1136 Figure 1: Schematic diagram of a possible tip zone deformation where the tips of two along-
 1137 strike faults overlap.

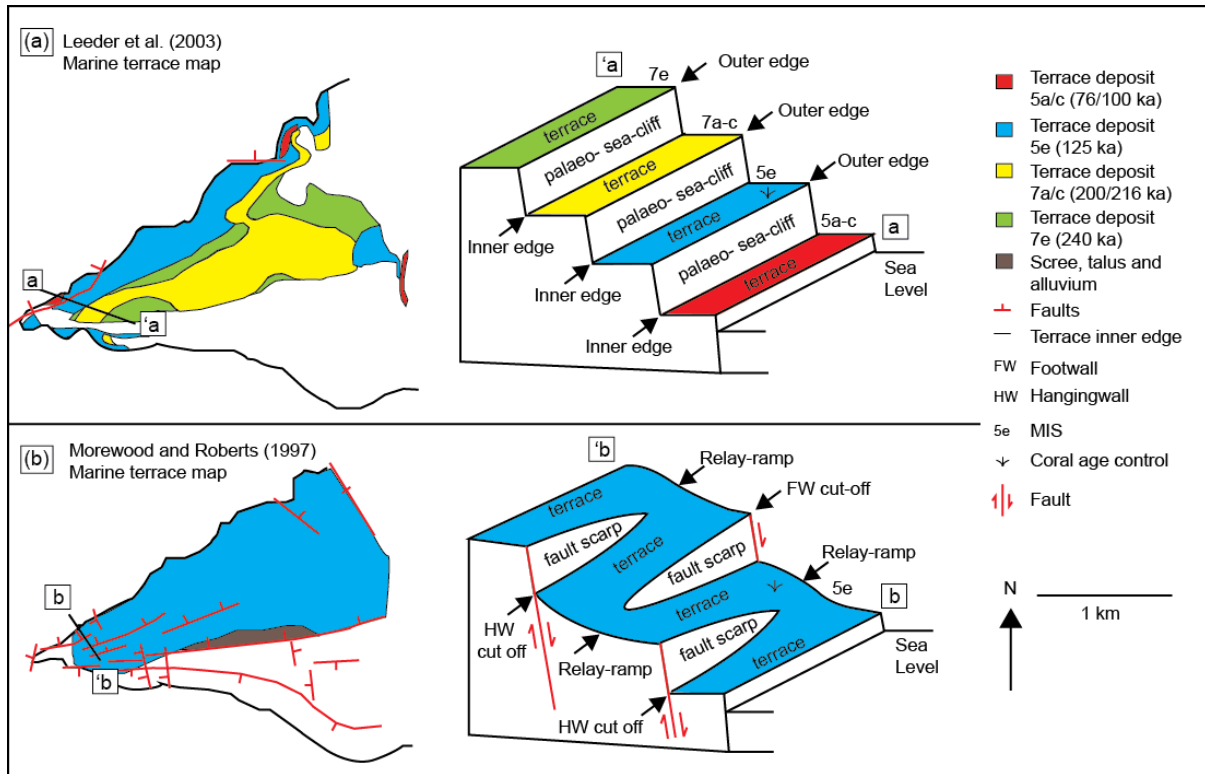


1138

1139 Figure 2: (a) Map of the eastern Gulf of Corinth and the Perachora Peninsula, surface trace
 1140 of the South Alkyonides Fault system (SAFS) (red) (Morewood and Roberts, 2002), East
 1141 Xylocastro Fault System (EXFS) trace (Bold) as per Nixon et al., 2016, all other faults as per
 1142 Nixon et al., 2016. (b) Location of the Gulf of Corinth and Hellenic subduction trench taken
 1143 from Kreemer and Chamot-Rooke (2004), GPS data from Nocquet (2012). (c) 5 m Digital
 1144 Elevation Model showing the western surface trace of the SAFS as per Morewood and

1145 Roberts (2002) and Cape Heraion. 'A' marks the location of the 'on-fault' tip of the SAFS
 1146 (Morewood and Roberts, 1999).

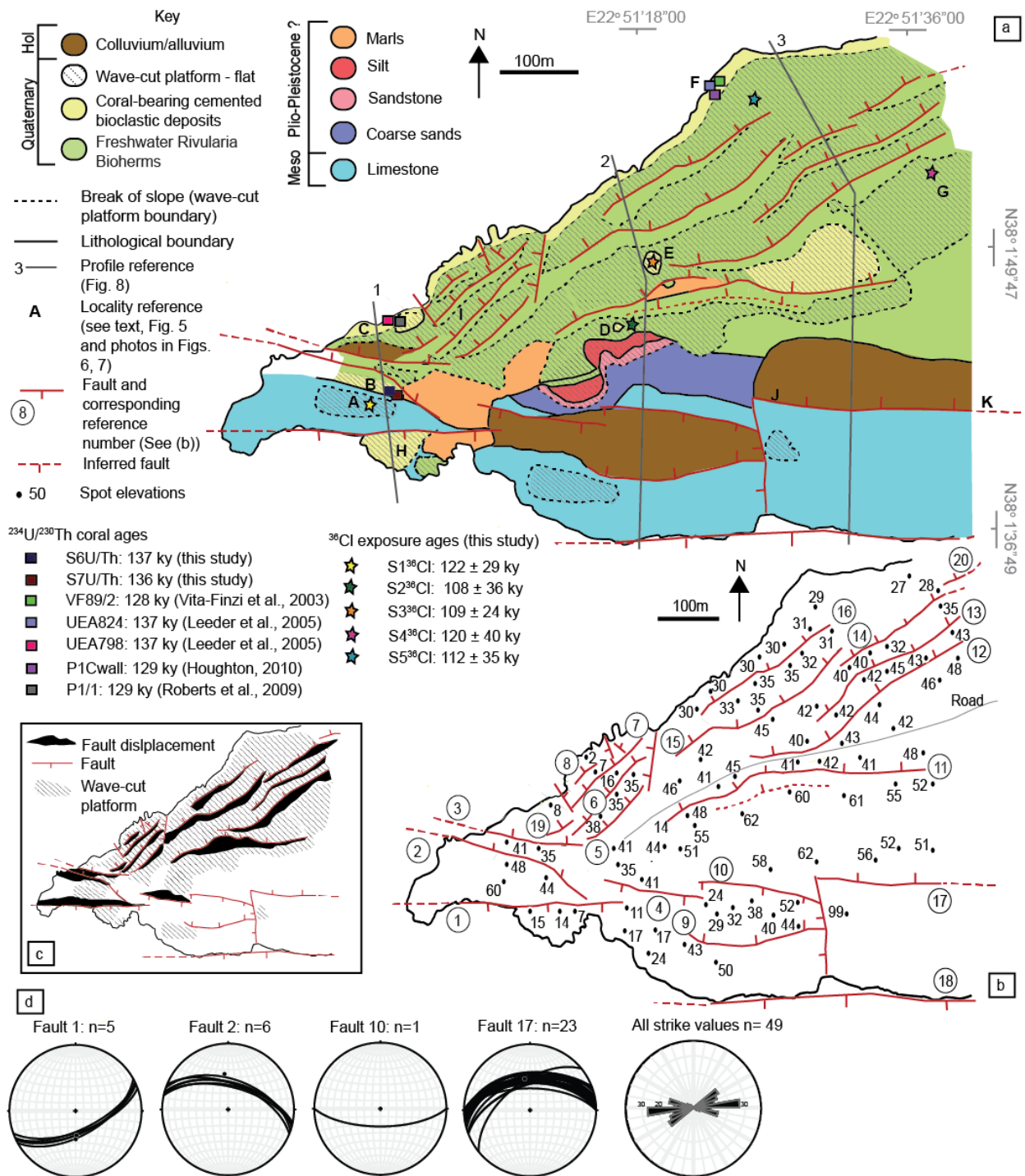
1147



1148

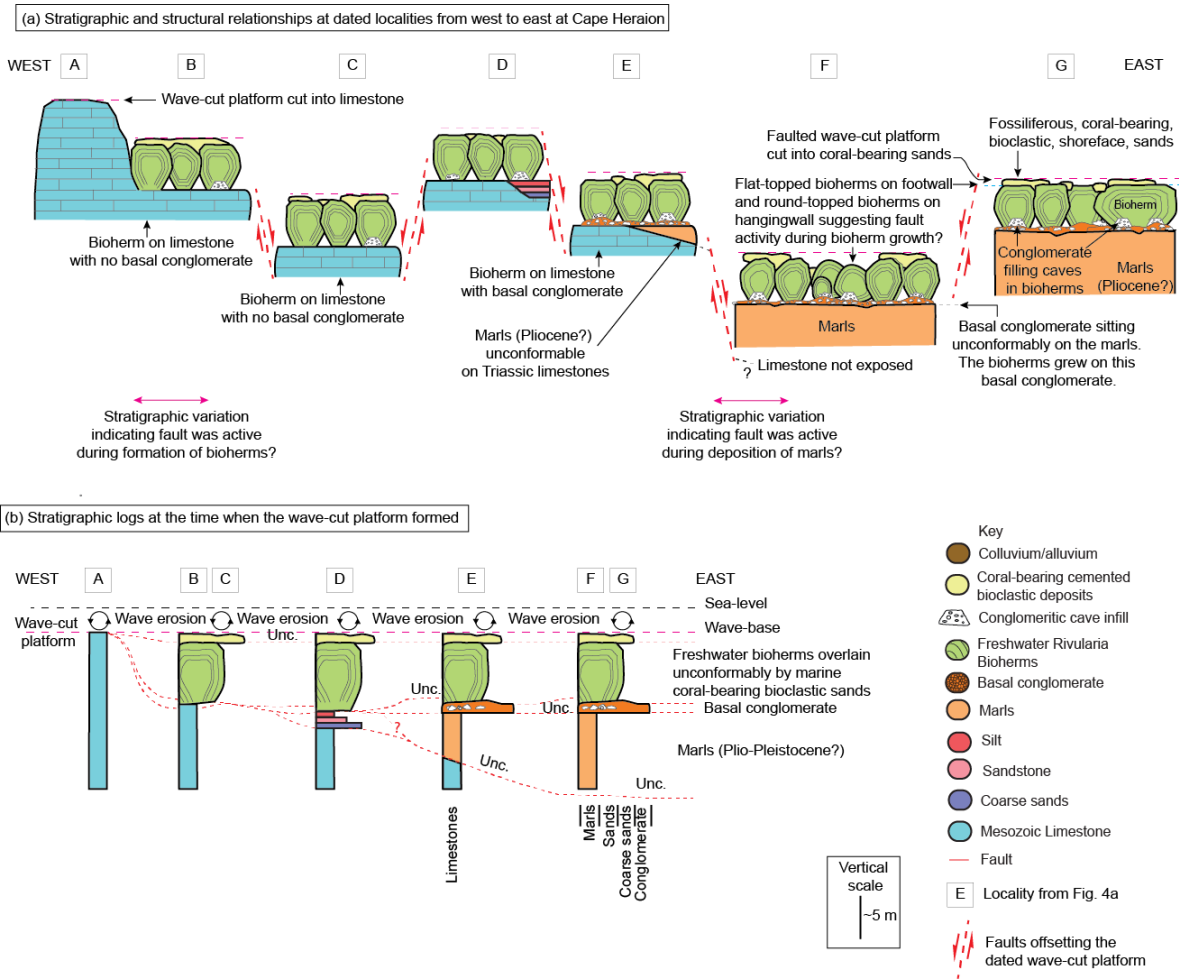
1149 Figure 3: Comparison of two explanations for the observed geomorphology on Cape
 1150 Heraion. (a) Geological map redrawn from Leeder et al. (2003) and interpreted schematic 3D
 1151 diagram, Leeder et al. (2003) suggest a sequence of palaeoshorelines from MIS 5a/c (76.5
 1152 ka/100 ka) to 7e (240 ka). (b) Geological map redrawn from Morewood and Roberts (1997)
 1153 and interpreted schematic 3D diagram, Morewood and Roberts (1997) suggest Cape
 1154 Heraion is linked to the MIS 5e 125 ka highstand and has been latterly faulted.

1155



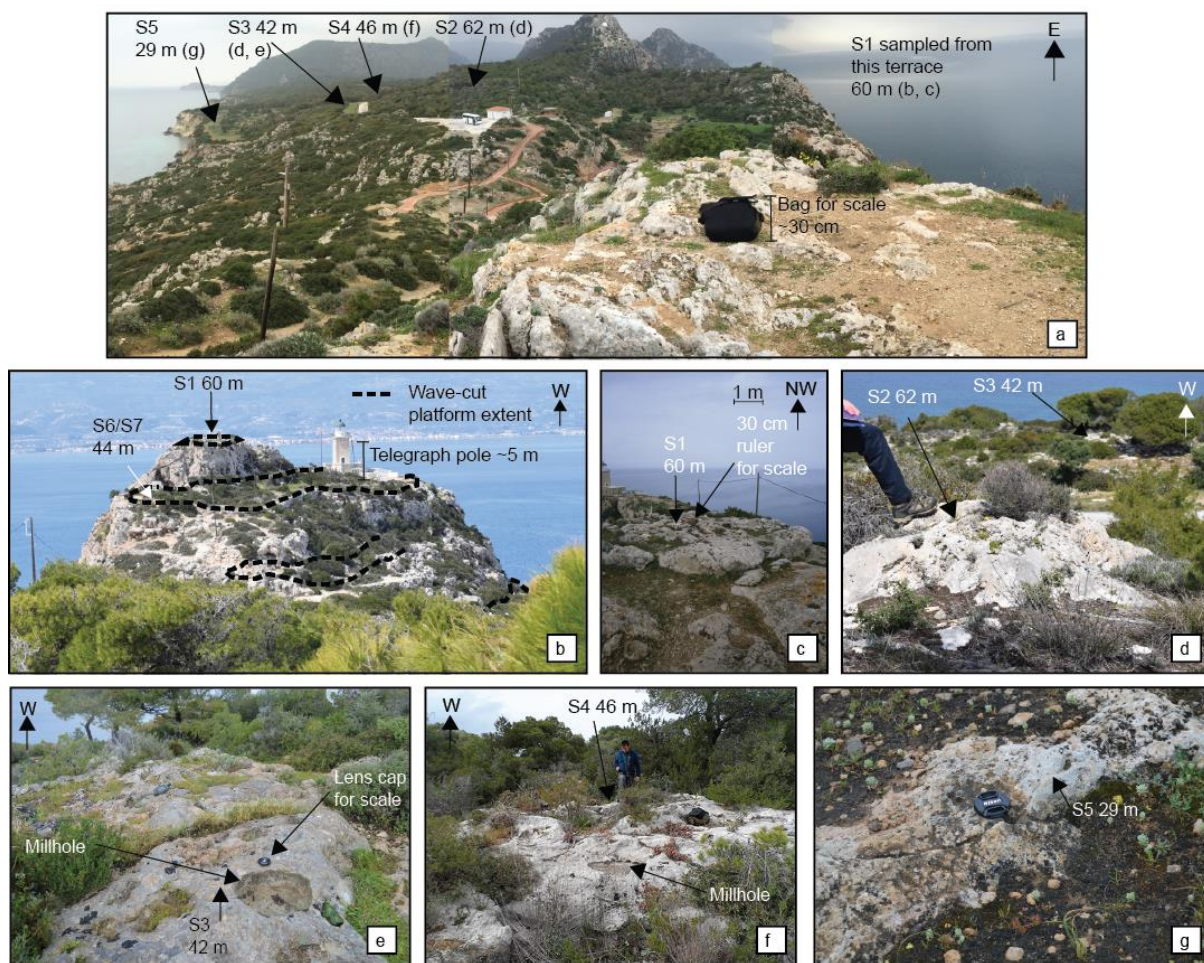
1156

1157 Figure 4: (a) Geological and geomorphological map of Cape Heraion, age controls from this
 1158 study and other coral studies (Vita-Finzi et al., 2003; Leeder et al., 2005; Roberts et al., 2009;
 1159 Houghton, 2010). (b) Fault map of Cape Heraion and spot height elevations used to plot the
 1160 fault displacement in (c). (d) Stereonet plots for faults 1, 2, 10 and 17, rose diagram
 1161 representing all measured strike values.



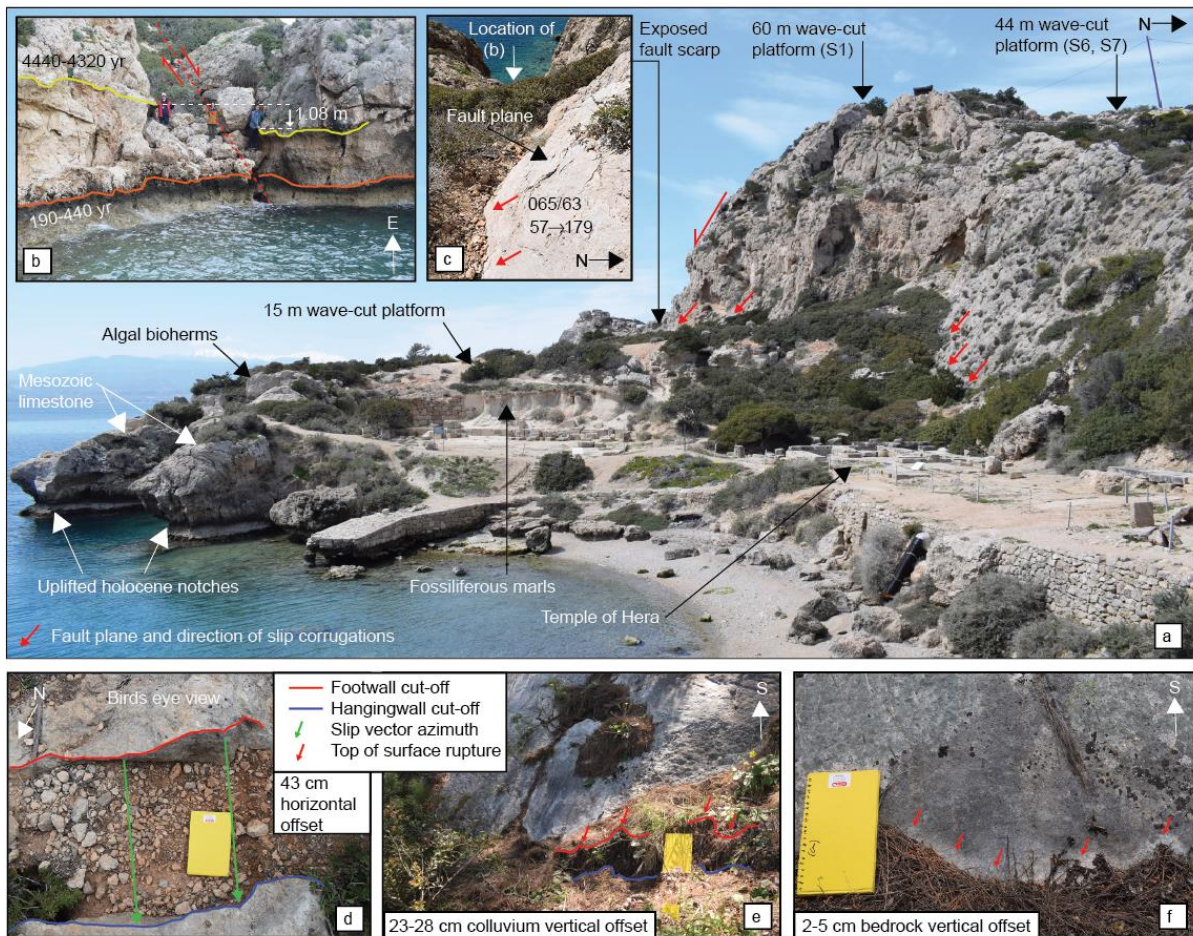
1162

1163 Figure 5: (a) Stratigraphic and structural relationships and (b) stratigraphic logs for dated
 1164 localities from West to East, see Figure 4 for localities



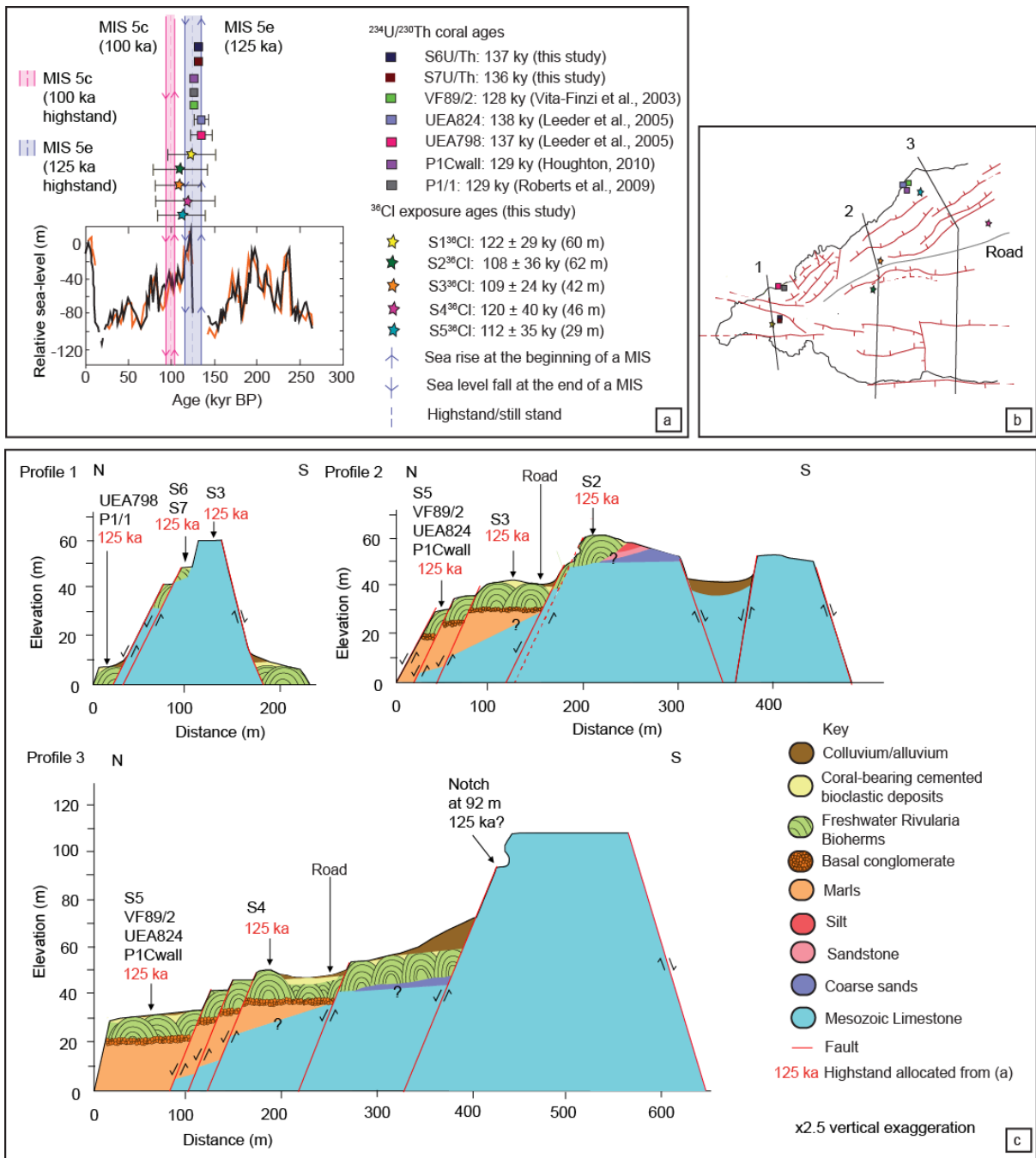
1165

1166 Figure 6: (a) overview of ^{36}Cl sample locations. (b-g) Photographs of ^{36}Cl and $^{234}\text{U}/^{230}\text{Th}$
 1167 sample locations. See Figure 4a for locations of samples.



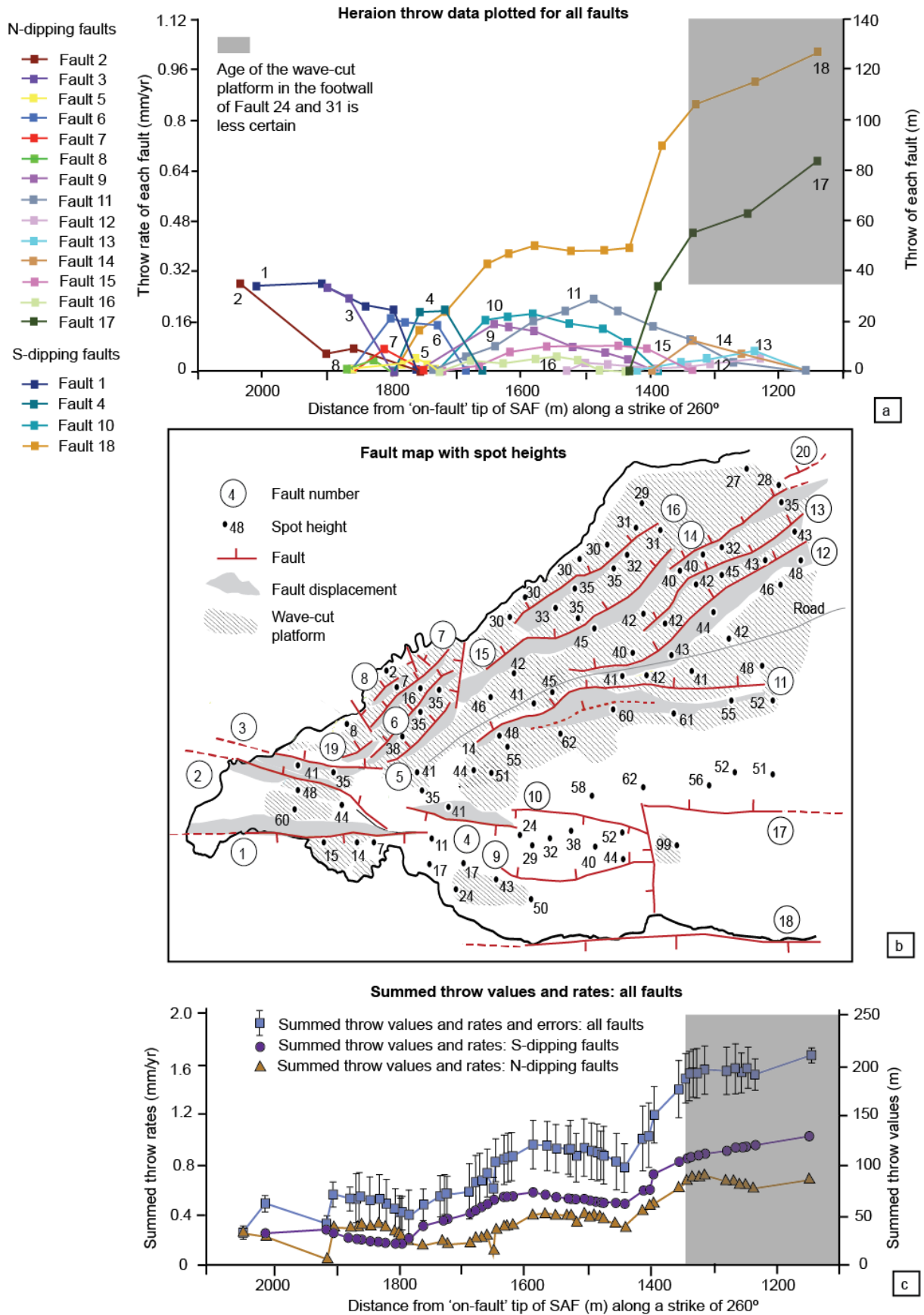
1168

1169 Figure 7: (a) View of Fault 1 offsetting a wave-cut platform at 60 m and 15 m. (b) Annotated
 1170 photograph of offset wave-cut notches on Fault 1. (c) Fault plane and annotated direction of
 1171 fault slip for Fault 1. (d) North-south horizontal offset of 43 cm on a bioherm on the north
 1172 side of Cape Heraion at Locality I, Figure 4. Offset colluvium (e) and bedrock (f) along fault
 1173 17 between localities J and K, Figure 4, UTM location: 663350/4210630.



1174

1175 Figure 8: (a) ^{36}Cl exposure ages and $^{234}\text{U}/^{230}\text{Th}$ coral ages (where error bars are not visible,
 1176 the value of error is smaller than the plot marker. Ages are plotted against the sea level
 1177 curve from Siddall et al., 2003, orange and black lines represent different cores used
 1178 to construct the sea-level curve. (b) Fault map and the location of profile lines from Figures 4a,
 1179 b that are shown as schematic cross sections in (c).

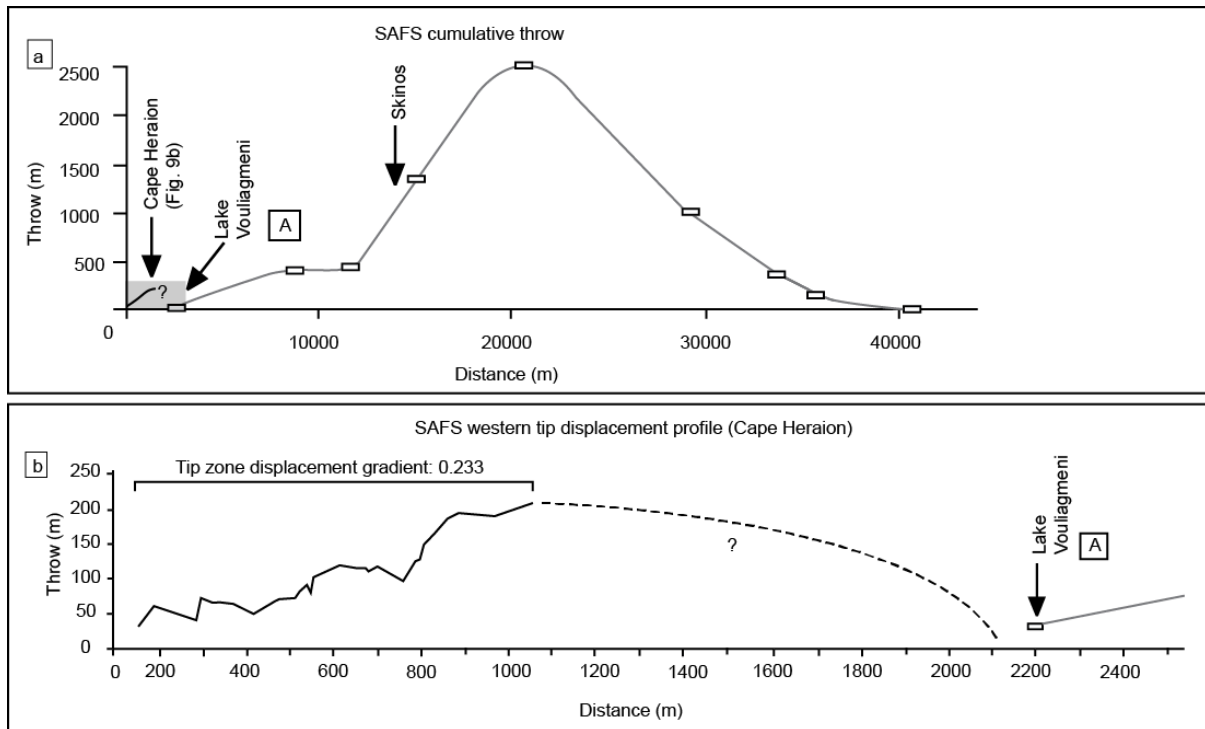


1180

1181 Figure 9: (a) Throw profiles for individual faults constructed using elevation data (shown in
 1182 (b)). Throw values for Fault 19 is not plotted owing to a lack of elevation data. (c) Summed

1183 throw values and rates for all faults with uncertainties, summed throw values for north- and
1184 south-dipping faults. For (a) and (c) throw for each fault is plotted against the distance from
1185 the 'on-fault' tip (A) shown in Figure 2c from Morewood and Roberts (1999).

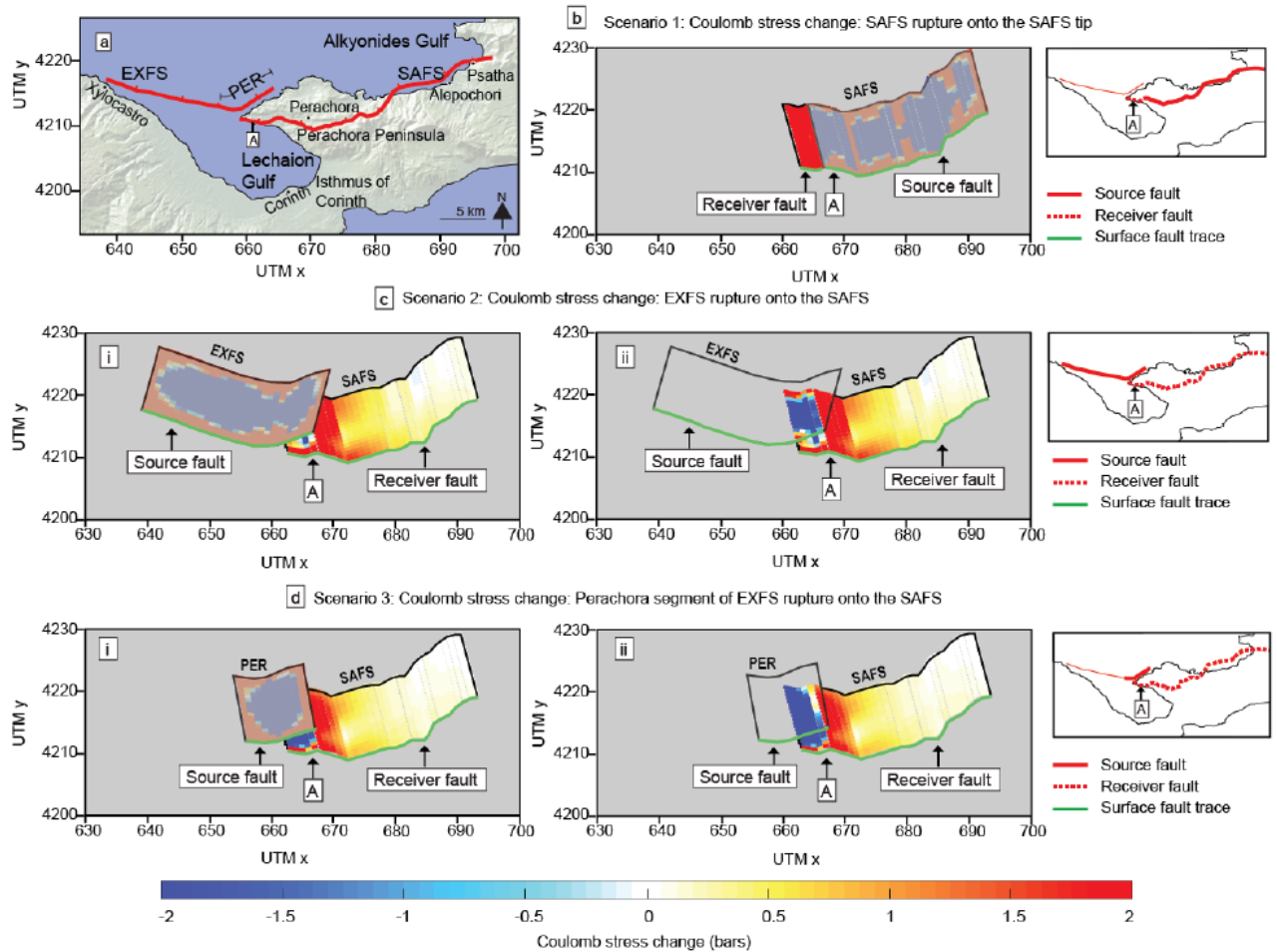
1186



1187

1188 Figure 10: (a) Summed throw of Cape Heraion faults plotted alongside cumulative throw of
1189 the SAFS (modified from Morewood and Roberts (1999)). (b) Tip zone throw and
1190 displacement gradient from Cape Heraion. See Figure 2c for the location of A ('on-fault' tip
1191 of the SAFS).

1192



1193

1194 Figure 11: (a) Map of eastern Gulf of Corinth showing the fault traces modelled in Coulomb
 1195 stress change (b-d) for the South Alkyonides Fault System (SAFS) and East Xylocastro Fault
 1196 System (EXFS) (adapted from Figure 2a). See table 4 for inputs into Coulomb modelling. (b)
 1197 Coulomb stress change from rupturing the source fault (entire SAFS with the exception of
 1198 the western 5 km) onto the receiver fault (western 5 km section of the SAFS). (c) Coulomb
 1199 stress change from rupturing the source fault (entire EXFS) onto the receiver fault (SAFS), (i)
 1200 shows the source fault rupture, (ii) shows the source fault outline only. (d) Coulomb stress
 1201 change from rupturing the source fault (Perachora segment of the EXFS) onto the receiver
 1202 fault (SAFS), (i) shows the source fault rupture, (ii) shows the source fault outline only.

1203

Fault number	d/L ratio
4	0.27
5	0.04
6	0.10
7	0.06
8	0.08
9	0.05
10	0.08
11	0.04
12	0.01
13	0.02
14	0.06
15	0.03
16	0.03

1204

1205 Table 1: displacement length (d/L) ratios for mapped faults on Cape Heraion, with the
 1206 exception of Fault 19 due to a lack of elevation data and Faults 1, 2, 3, 17, 18, 20 as both tips
 1207 could not be mapped.

Sample name	Lab ID	UTM		Sampling elevation (m)	Age (ky)	$\pm 2s$ (abs) (ky)	U (ppm)	^{232}Th (ppb)	$^{232}\text{Th}/^{238}\text{U}$	$\pm 2s$ (%)
		Easting	Northing							
S6U/Th (1)	138-34	662540	4210594	44	133.5	0.747	2.42	0.005	0.0006756	0.04
S6U/Th (2)	141-29	662540	4210594	44	135.4	1.248	2.44	0.006	0.0007647	0.12
S6U/Th (3)	141-30	662540	4210594	44	142.7	1.277	2.57	0.006	0.0007943	0.10
S6U/Th (4)	145-12	662540	4210594	44	173.7	1.954	2.13	0.009	0.0013646	0.17
S7U/Th (1)	138-35	662540	4210594	44	140.8	0.756	2.26	0.008	0.0011359	0.04
S7U/Th (2)	145-13	662540	4210594	44	139.1	0.887	2.28	0.012	0.0017902	0.08
S7U/Th (3)	145-14	662540	4210594	44	135.2	0.967	2.24	0.009	0.0013667	0.10
S7U/Th (4)	145-15	662540	4210594	44	134.5	0.996	2.34	0.014	0.0019207	0.11
S7U/Th (5)	145-16	662540	4210594	44	134.7	0.876	2.13	0.008	0.0012517	0.09
S7U/Th (6)	145-17	662540	4210594	44	132.3	0.947	2.39	0.016	0.0022281	0.08

1208

Sample name	$\pm 2s$ (%)	$^{230}\text{Th}/^{238}\text{U}$	$\pm 2s$ (%)	$^{234}\text{U}/^{238}\text{U}$ Activity ratio	$\pm 2s$ (%)	Initial $^{234}\text{U}/^{238}\text{U}$ Activity	$\pm 2s$ (%)	Converted to $\delta 234\text{U}$ (‰)
S6U/Th (1)	0.04	0.81787	0.25	1.1354	0.14	1.1975	± 0.002	197
S6U/Th (2)	0.12	0.82081	0.35	1.1315	0.28	1.1927	± 0.004	193
S6U/Th (3)	0.10	0.85306	0.34	1.1429	0.25	1.2139	± 0.004	214
S6U/Th (4)	0.17	0.92101	0.34	1.1287	0.29	1.2103	± 0.005	210
S7U/Th (1)	0.04	0.83619	0.22	1.1298	0.13	1.1933	± 0.002	193
S7U/Th (2)	0.08	0.83630	0.25	1.1359	0.18	1.2015	± 0.003	201
S7U/Th (3)	0.10	0.81931	0.29	1.1301	0.21	1.1907	± 0.003	191
S7U/Th (4)	0.11	0.81943	0.29	1.1328	0.22	1.1943	± 0.003	194
S7U/Th (5)	0.09	0.82413	0.26	1.1380	0.19	1.2020	± 0.003	202
S7U/Th (6)	0.08	0.81141	0.29	1.1315	0.21	1.1913	± 0.003	191

1209

1210 Table 2: $^{234}\text{U}/^{230}\text{Th}$ coral age dating analytical results for samples S6U/Th and S7U/Th (see
1211 Figure 4a for sample location). Activity ratios calculated using the ^{234}U and ^{230}Th decay
1212 constants of Cheng et al. 2013. Activity ratios corrected for ^{230}Th , ^{234}U and ^{238}U
1213 contribution from the synthetic ^{236}U - ^{229}Th tracer, instrument baselines, mass bias,
1214 hydride formation and tailing. ^{230}Th blanks amounting to 0.15 ± 0.03 fg were subtracted
1215 from each sample. ^{238}U blanks were on the order of 10 pg, and were negligible relative to
1216 sample size. Age and $\delta 234\text{U}$ data were corrected for the presence of initial ^{230}Th assuming
1217 an initial isotope composition of $(^{232}\text{Th}/^{238}\text{U}) = 1.2 \pm 0.6$, $(^{230}\text{Th}/^{238}\text{U}) = 1 \pm 0.5$ and
1218 $(^{234}\text{U}/^{238}\text{U}) = 1 \pm 0.5$ (all uncertainties quoted at the 2σ level).

Sample name	Lithology and geomorphology	Latitude	Longitude	Elevation	Lithology
1	Limestone, flat WCP with lithophagid borings	38.0288	22.85106	60	Limestone
2	Bioherm top, bioclastic sands infill spaces between adjacent bioherms	38.0292	22.85297	62	Bioherm
3	Bioclastic packstone, excellent millholes preserved	38.0304	22.85522	42	Packstone
4	Bioherm top, abundant millholes, lithophagid borings preserved	38.032	22.8596	46	Bioherm
5	Bioherm top, visible above surrounding alluvium	38.0305	22.85516	29	Bioherm

1219

Sample name	Erosion rate (mm/ky)	Total erosion (cm)	Cl (ppm)	\pm	^{36}Cl (atoms/g)	\pm	CaO (wt%)	\pm	Age (kyr)	Internal uncertainty (kyr)	External uncertainty (kyr)
1	0.1	12.5	17.05027	0.2856176	2327699	63421	57.41238	1.38	122	3.7146	29
2	5	625	22.5328	0.4739153	1195064	34923	43.84561	1.53	108	8.3772	36
3	0.1	12.5	38.77938	0.8002648	1887336	54970	49.01585	1.52	109	3.5001	24
4	5	625	33.32635	0.6645615	1616569	47009	53.79968	1.47	120	8.7588	40
5	5	625	60.55609	1.6227309	1684932	46140	54.01351	1.44	112	9.3003	35

1220

1221 Table 3: ^{36}Cl exposure dating analytical results and sample descriptions (see Figure 4a for
1222 the sample location).

Fault name	Fault information (fault trace, kinematics)	Length (km)
East Xylocastro Fault System (EAFS)	Whole fault length is used combining fault traces of the East Xylocastro Fault, North Kiato Fault and Perachora Fault as per Nixon et al., 2016.	29
Perachora Fault (EXFS)	Fault trace from Nixon et al., 2016	11
South Alkyonnides Fault System (SAFS)	Whole fault length is used as per Roberts et al., 2009 (rupturing the Pisias, East Alkyonides and Psatha faults), with the exception of western 5 km tip zone. Dip data averaged from Jackson et al., 1982 (45°) and Mechernich et al., 2016 (60°)	38.7

1223

Fault name	Depth of seismogenic	Dip °	Facing direction °	Rake °	Sub-surface maximum slip	Max. Mw	Figure
East Xylocastro Fault System (EAFS)	15	55	010	-90	1.6	6.53	10b
Perachora Fault (EXFS)	15	55	350	-90	1.4	6.21	10c
South Alkyonnides Fault System (SAFS)	15	55	345	-90	2.4	6.74	10a

1224

1225 Table 4: Inputs for Coulomb stress change modelling. Slip at the surface is set at 0.1 (10%) of
 1226 the slip value at depth. This value is based upon the relationship between surface slip
 1227 (Vittori et al., 2011) and maximum slip values at depth (Wilkinson et al., 2015) for the Mw
 1228 6.3 2009 L'Aquila Earthquake, Italy.

1229 **Appendix one:**

1230 Description of the observed stratigraphy on Cape Heraion to accompany Figures 4a and 5)

1231

1232 At the base of the stratigraphic column is Mesozoic limestone (Figures 4a, 5, Locality
 1233 A). Unconformably above the limestone is a sedimentary succession, only observed in the
 1234 centre of the cape, that fines up from coarse sands to silts (Locality D, Figure 4a and Figure 5).
 1235 Plio-Pleistocene marls are inferred to occur stratigraphically above the sands and silts
 1236 although the contact between them has not been observed, and they may be lateral
 1237 equivalents. The marls form large cliff outcrops along the north of the cape (e.g. Locality F in
 1238 Figures 4 and 5) and are overlain by a coarse boulder conglomerate that displays an erosive
 1239 base cut into the underlying marls (Locality F). Algal carbonate bioherms formed of *Rivularia*
 1240 *haematities* have grown on the basal conglomerate (Localities E, F and G, Figure 5) and
 1241 directly on the basement limestone (Localities B, C and D, Figure 5). In turn, the bioherms are

1242 overlain by fossiliferous, coral-bearing, marine bioclastic sands preserved as a continuous 0.6-
1243 1.0 m thick layer (Localities B, C, E, F and H, Figures 4a, 5) or as patches infilling cavities
1244 between or within the bioherms (Locality C and D Figure 4a, 5). These bioclastic deposits have
1245 rich fossil assemblages with colonies of the branching coral *Cladocora caespitosa* in life
1246 position, frameworks of serpulid worm tubes, and bivalves, pecten, turritella, bryozoa, and
1247 elsewhere broken fragments of *Cladocora caespitosa* within the sediment that form death
1248 assemblages. In places, the inside of the bioherms has been eroded and small caves have
1249 formed, which have been bored by lithophagids (Figure 5). The caves contain marine deposits
1250 such as *Cladocora caespitosa* (e.g. Locality C), suggesting the cave-filling deposits are the age-
1251 equivalents of the coral-bearing bioclastic sands that lie on top of the bioherms.

1252

1253